

See discussions, stats, and author profiles for this publication at: <https://www.researchgate.net/publication/283225174>

Euxinic conditions recorded in the ca. 1.93 Ga Bravo Lake Formation, Nunavut (Canada): Implications for oceanic redox evolution

Article in *Chemical Geology* · June 2015

DOI: 10.1016/j.chemgeo.2015.09.004

CITATIONS

4

READS

209

4 authors, including:



Camille A. Partin

University of Saskatchewan

24 PUBLICATIONS 292 CITATIONS

SEE PROFILE



Andrey Bekker

University of California, Riverside

183 PUBLICATIONS 6,466 CITATIONS

SEE PROFILE



Timothy W. Lyons

University of California, Riverside

351 PUBLICATIONS 12,476 CITATIONS

SEE PROFILE

Some of the authors of this publication are also working on these related projects:



Trace metal proxies [View project](#)



Permian-Triassic boundary [View project](#)



Euxinic conditions recorded in the ca. 1.93 Ga Bravo Lake Formation, Nunavut (Canada): Implications for oceanic redox evolution



C.A. Partin^{a,*}, A. Bekker^b, N.J. Planavsky^c, T.W. Lyons^b

^a Department of Geological Sciences, University of Saskatchewan, 114 Science Place, Saskatoon, SK S7N 5E2, Canada

^b Department of Earth Sciences, University of California, Riverside 92521, USA

^c Department of Geology and Geophysics, Yale University, New Haven, CT 06520, USA

ARTICLE INFO

Article history:

Received 16 April 2015

Received in revised form 3 September 2015

Accepted 4 September 2015

Available online 12 September 2015

Keywords:

Paleoproterozoic
Ocean redox state
Paleo-redox
Trace metals
Euxinia
Black shales
Canadian Shield

ABSTRACT

The composition of seawater changed dramatically during the initial rise of atmospheric oxygen in the earliest Paleoproterozoic, but the emerging view is that atmosphere–ocean system did not experience an irreversible transition to a well-oxygenated state. Instead, it has been suggested that the oxygen content of the atmosphere–ocean system decreased considerably after ca. 2.06 billion years ago (Ga), which resulted in a crash in marine sulfate concentrations. The end of the deposition of major granular iron formations at ca. 1.85 Ga has been linked either to the development of extensive euxinic conditions along continental shelves or a decrease in hydrothermal flux. The record of oceanic redox state is not well constrained for the period between ca. 2.06 Ga, the end of the Lomagundi positive carbon isotope excursion, and ca. 1.88 Ga when major granular iron formations appeared. We address this gap by presenting new iron-speciation, major and trace element data, as well as sulfur, organic carbon, and molybdenum isotopic data for greenschist facies organic matter-rich mudrocks (ORMs) of the ca. 1.93 Ga Bravo Lake Formation, Piling Group, Baffin Island. The iron speciation data suggest deposition of the Bravo Lake Formation under a euxinic (anoxic and sulfidic) water column. Trace metal enrichments and Mo isotope data suggest extensive marine euxinia ca. 90 million years before the disappearance of large-scale, economic granular iron formations. The addition of new Mo data in this time interval is important, as it contributes to filling in the sparse Proterozoic record. Lastly, this work provides further support for the idea that there was widespread anoxia shortly after the end of the Lomagundi Event.

© 2015 Elsevier B.V. All rights reserved.

1. Introduction

There are few constraints on the chemical composition and redox conditions of late Paleoproterozoic seawater from ca. 2.06 to 1.88 Ga. In the wake of the Great Oxidation Event (GOE) that started between 2.47 and 2.32 Ga, the chemistry and redox architecture of seawater changed dramatically. The oxidation of continental rocks, containing redox-sensitive minerals such as sulfides, brought an influx of sulfate and redox-sensitive trace elements to the oceans (e.g., Holland, 1984; Scott et al., 2008, 2014; Konhauser et al., 2011). An increase in the range of sulfur isotope data by 2.4 to 2.3 Ga is also consistent with greater fractionation favored by higher levels of seawater sulfate (e.g., Canfield, 1998). Recent documentation of large fluctuations in the oxygen content of the atmosphere–ocean system, particularly after ca. 2.06 Ga, demonstrates that the Earth experienced a dynamic history of oxygenation prior to its stabilization to higher O₂ levels by the Phanerozoic (Bekker and Holland, 2012; Planavsky et al., 2012; Canfield et al., 2013; Partin et al., 2013; Lyons et al., 2014).

After the initial rise during the GOE, atmospheric oxygen levels were sustained by a large and long-lived organic carbon burial event. Paleoproterozoic carbonate successions bracketed in age between ca. 2.22 and 2.06 Ga worldwide host the largest and longest-lived positive carbon isotope excursion recorded in Earth's history, the so-called Lomagundi Event (Karhu and Holland, 1996; Melezhik et al., 1999; Bekker et al., 2001), with typical $\delta^{13}\text{C}$ values up to +10 to +12‰ (Karhu and Holland, 1996). The Lomagundi Event is thought to be the expression of a ca. 140 million-year organic carbon burial event of unprecedented and unrepeated magnitude. Estimated extent of organic carbon burial would have resulted in a large influx of oxygen to the atmosphere, perhaps over 20 times the present atmospheric inventory (Karhu and Holland, 1996). Some of this oxygen was likely consumed during the large-scale oxidation of continental crust (Konhauser et al., 2011; Kump et al., 2011), while some likely accumulated in the atmosphere and oceans (e.g., Partin et al., 2013). Whatever the redox texture of the atmosphere–ocean system was during that time, this enhanced oxygen and organic carbon production markedly influenced the composition of contemporaneous seawater. The fate of organic carbon buried during the Lomagundi Event might have a particular bearing on the redox state of the deep oceans in the aftermath of this event (e.g., Kump et al., 2011). The oxidation of this organic carbon could

* Corresponding author.

E-mail address: camille.partin@usask.ca (C.A. Partin).

have resulted in a less oxidizing atmosphere and the expansion of euxinic conditions (Canfield et al., 2013). Alternatively, it has been proposed that ca. 1.93 to 1.88 Ga seawater was dominated by ferruginous conditions (Bekker et al., 2010), as large iron formations began to reappear in the geologic record after a long hiatus during the GOE and Lomagundi Event, culminating with the peak in abundance of granular iron formations at ca. 1.88 Ga (Rasmussen et al., 2012). Deposition of granular iron formations at ca. 1.88 Ga implies the transport of Fe^{2+} to near-shore environments, which requires low atmospheric oxygen levels (Holland, 2003; Canfield, 2005). This relationship is in direct contrast to high atmospheric and surface-ocean oxygen levels inferred for the preceding GOE and Lomagundi Event intervals (ca. 2.4 to 2.06 Ga).

There is mounting evidence for high seawater sulfate concentrations between ca. 2.22 and 2.06 Ga (Schröder et al., 2008; Planavsky et al., 2012; Reuschel et al., 2012b; Scott et al., 2014), and possibly even as early as 2.32 Ga (Bekker et al., 2004; Scott et al., 2014), and a rapid contraction of seawater sulfate levels thereafter (Planavsky et al., 2012; Scott et al., 2014). The increase in seawater sulfate concentrations is related to the onset of the GOE and the Lomagundi Event, whereas the decrease in seawater sulfate concentrations coincides with the end of the Lomagundi Event. A lack of Paleoproterozoic sulfate evaporites in successions younger than ca. 2.1 Ga (Schröder et al., 2008; Scott et al., 2014) is consistent with a crash in seawater sulfate concentrations, as is documented for the ca. 1.9 Ga Stark Formation, which lacks the evaporite sequence from gypsum to halite (Pope and Grotzinger, 2003). Lower sulfate levels are also inferred for the mid-Proterozoic in general until ca. 1.1 Ga or even later (e.g., Canfield et al., 2010; Scott et al., 2014).

With only limited snapshots available, the redox state of the ocean in the time interval from ca. 2.06 to 1.88 Ga is still poorly constrained. It is likely that the oceans returned to a lower oxidation state following the end of the Lomagundi Event, but few datasets speak to this transition. Thus, there is a need for marine sedimentary successions in this time interval that can elucidate surface oxygen levels and marine redox structure.

In this study, we aim to fill this knowledge gap for the redox state of the Paleoproterozoic oceans by contributing new iron speciation, major and trace elements, and sulfur, organic carbon, and molybdenum isotope data from greenschist-facies organic matter-rich mudrocks (ORMs) of the ca. 1.93 Ga Bravo Lake Formation (BLF), Piling Group, Baffin Island. Though the BLF experienced a higher metamorphic grade conditions than is typically sought after for geochemical studies, we make a case that these ORM archives still provide important insights into a poorly constrained, but geochemically dynamic interval in the redox history of the atmosphere–ocean system.

2. Geological setting

Sedimentary basins were formed on the Rae craton as a result of regional crustal extension, followed by renewed subsidence related to regional compressional tectonic events around the Rae craton (Aspler et al., 2001; Rainbird et al., 2010), particularly the ca. 1.88 Ga Foxe orogeny, the ca. 1.92 to 1.8 Ga Trans-Hudson orogeny (Corrigan et al., 2009), and the 2.0 to 1.90 Ga Taltson–Thelon orogeny (Hanmer et al., 1992). The <2.16 Ga to >1.897 Ga Piling Group was deposited along the southeastern margin of the Rae craton in an epicontinental basin that transitioned to a foreland basin setting in response to the Foxe orogeny, which involved the continent–continent collision of the Meta Incognita microcontinent and Rae craton (Fig. 1; Partin et al., 2014). The lower Piling Group, in ascending stratigraphic order, consists of the Dewar Lakes Formation, which rests unconformably on the Archean basement as a thinly bedded micaceous quartzarenites, the dolomitic and calcitic carbonates of the Flint Lake Formation, followed by the mudstone/siltstone of the Astarte River Formation (Fig. 2). Flint Lake Formation carbonates do not show ^{13}C -enrichments indicative of the Lomagundi Event, suggesting deposition of the lower Piling Group after ca. 2.06 Ga (Partin et al., 2014). The Flint Lake and Astarte River formations

occur exclusively in northern Piling Group exposures, whereas the Dewar Lakes Formation is present in both northern and southern exposures of the Piling Group. The BLF lies stratigraphically above the Dewar Lakes Formation in southern exposures of the Piling Group. The BLF consists of a sequence of alkaline, tholeiitic, and intermediate basalts extruded in a submarine environment and intercalated with coarse- to fine-grained sandstones, lithic wackes, and minor ORM. The Longstaff Bluff Formation overlies the lower Piling Group in northern and southern exposures and occurs both stratigraphically above and intercalated with the BLF, suggesting a conformable transition. The stratigraphic thickness of the Piling Group is estimated to be 5–7 km (Tippett, 1978; Scott et al., 2002). The central part of the Piling Group outcrop belt, which includes the BLF, experienced greenschist facies metamorphism (between 400 and 500°C; Partin et al., 2014), though metamorphic grade increases to the north and south (Corrigan et al., 2001; Gagné et al., 2009). The Piling Group experienced variable tectonic strain during the Foxe orogeny (Gagné et al., 2009). We discuss several geochemical parameters to assess the potential impact of metamorphism and hydrothermal fluids on the BLF (Section 5.5).

Deposition of the Longstaff Bluff Formation is interpreted to have occurred in a pro-foreland basin (Partin et al., 2014). Volcanism within the BLF coincides with the earliest phase of foreland basin development and is interpreted as early foredeep magmatism (Partin et al., 2014). A shallow-marine depositional environment is inferred for the BLF based on volcanic structures and textures that demonstrate extrusion in a low-pressure environment (<1–2 km water depth; Johns et al., 2006), with variable energy conditions as shown by trough cross-bedding in wackes stratigraphically below the ORM interval. We interpret the Bravo Lake Formation to represent a shallow shelf environment. From a basin evolution standpoint, we argue that the Piling basin was not appreciably restricted from the open ocean during deposition of the BLF, since there was local rift-related extension during the early phase of foreland basin development on a continental margin (Partin et al., 2014).

The minimum age of the Piling Group is constrained by a $1897 \pm 7/-4$ Ma (U–Pb age) K-feldspar megacrystic monzogranite pluton that contains psammite enclaves interpreted to belong to the upper Piling Group (Wodicka et al., 2002). A differentiated gabbro-granodiorite sill dated at $1897 \pm 10/-5$ Ma (U–Pb age) that intrudes the BLF also supports this minimum age constraint. A trachyte dyke dated at 1923 ± 15 Ma (U–Pb age; Wodicka et al., 2014) within the BLF is geochemically similar to the upper volcanic sequence of the BLF and might better represent the age of volcanism and deposition. The youngest detrital zircon in a lithic metawacke of the BLF suggests a maximum U–Pb age of deposition around 1940 Ma (Partin et al., 2014). Thus, the deposition of the BLF is younger than ca. 1.94 Ga, but older than ca. 1.92 Ma, with an interpreted age of ca. 1.93 Ga. Samples analyzed in this study were obtained from drill core from the Ridges Lake area on Baffin Island and represent an approximately seven-meter-thick section of unweathered sulfide-bearing ORM (Fig. 1).

3. Methods

3.1. Sulfur isotope analysis

Core samples were powdered using an agate mill prior to analysis. Sulfur from sulfides (pyrite, and pyrrhotite) in each sample was extracted and converted to Ag_2S using the chromium reduction method (Canfield et al., 1986). Sulfur isotope analyses of Ag_2S were performed at SIFIR Laboratory, University of Manitoba. Approximately 0.2–0.4 mg of sample powder was weighed into Sn cups (5×3.5 mm), sealed and analyzed for S isotope ratios using a Costech 4010 Elemental Analyzer (EA) coupled to a Thermo Finnigan Delta V Plus isotope-ratio mass spectrometer (IRMS) via an open-split interface (ConFlo IV, Thermo Finnigan). Calibration was performed by analyzing three international Ag_2S standards (IAEA-S1, IAEA-S2, and IAEA-S3) at the beginning, middle and end of each run. A calibration line was calculated by least squares

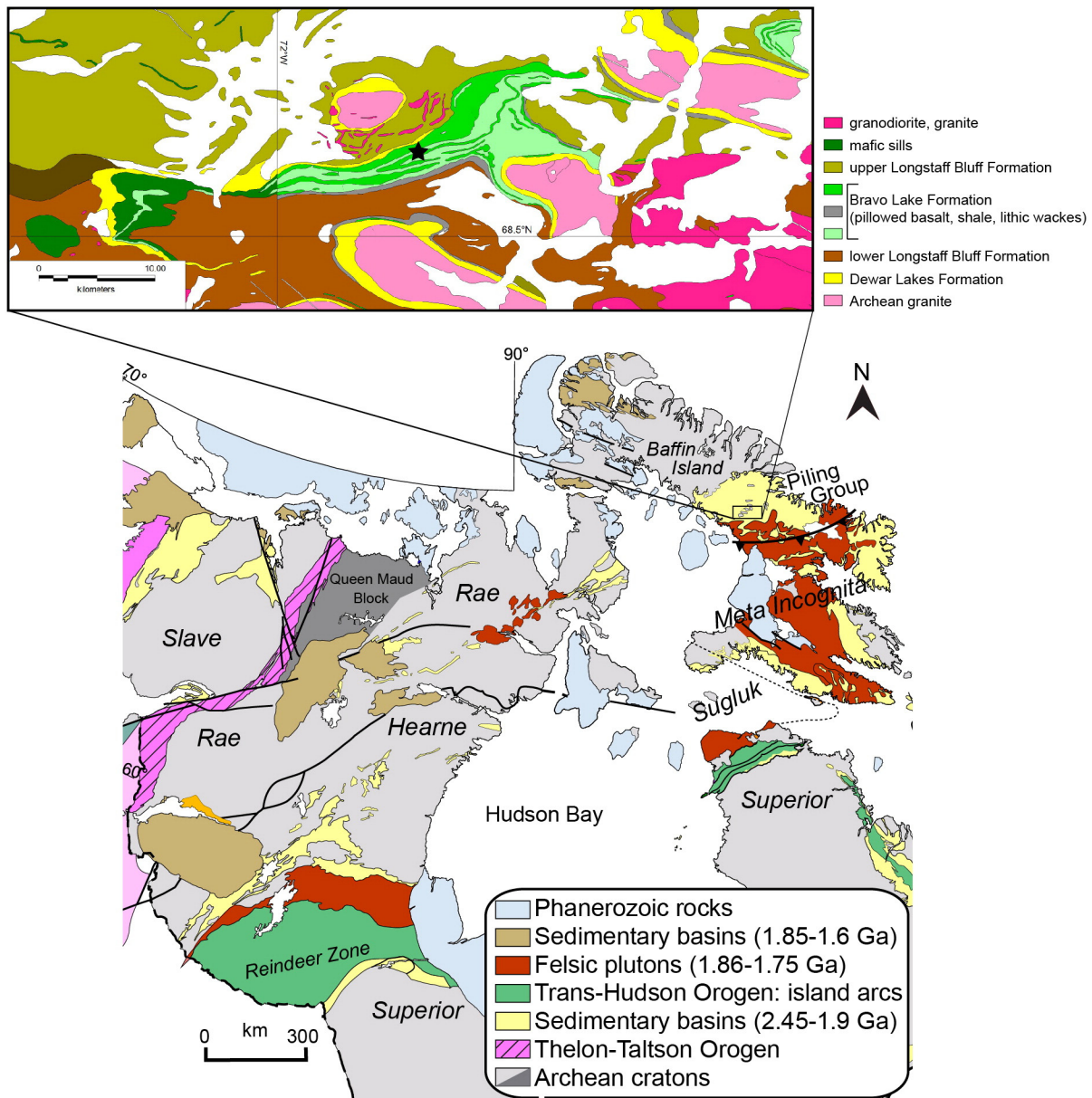


Fig. 1. Location and geologic setting of the Bravo Lake Formation on Baffin Island, Canada (lower figure is modified after Corrigan et al., 2009). Inset box (upper) provides the detailed geology of the Bravo Lake Formation in the Ridges Lake area; the star marks the location of the drill core site at -68.675°N , 71.875°W .

linear regression using the known and measured isotope values of the calibration standards. To monitor the quality of analysis performance, one sulfide internal standard (Maine Light) was analyzed with our samples, with the result of $\delta^{34}\text{S} = -31.1 \pm 0.3\%$ ($n = 6$). Error on $\delta^{34}\text{S}$ analyses is $\pm 0.2\text{--}0.3\%$. $\delta^{34}\text{S}$ values are reported relative to Vienna–Canyon Diablo Troilite (V-CDT).

3.2. Organic carbon isotope analysis

ORM samples were prepared via decarbonation by treatment with 6 N HCl for seven days prior to the analysis. Organic carbon isotope analysis was completed using a Costech 4010 Elemental Analyzer (EA) attached to a Delta V Plus mass-spectrometer at the University of Manitoba. Calibration was performed by analyzing two international standards (USGS40, USGS41) at the beginning, middle and end of each run following Coplen et al. (2006). A calibration line was calculated by least squares linear regression using the known and measured isotope values of the calibration standards. To monitor the quality of sample

preparation (decarbonation by HCl) and analysis performance, an international standard USGS Green River shale SGR-1b ($\delta^{13}\text{C}_{\text{org}} = -29.3 \pm 0.1\%$ VPDB) (Dennen et al., 2006) was treated and analyzed with unknown samples. Replicate analyses of SGR-1b standard yielded the result of $\delta^{13}\text{C}_{\text{org}} = -29.6 \pm 0.04\%$ ($n = 6$).

3.3. Iron speciation analysis

A calibrated sequential extraction procedure (Poulton et al., 2004; Poulton and Canfield, 2005) was applied to samples of the BLF to determine the speciation of highly-reactive iron (Fe_{HR}), which includes iron now hosted in pyrite and other iron phases that would have reacted with sulfide to form pyrite either in the water column or during early diagenesis in sediments given sufficient exposure to H_2S . The following components were measured to determine Fe_{HR} . Carbonate-associated iron (e.g., siderite) (Fe_{carb}) was extracted by treatment of ~ 100 mg of powdered sample with a buffered sodium acetate solution. The sodium acetate extraction can also leach iron from monosulfides like pyrrhotite.

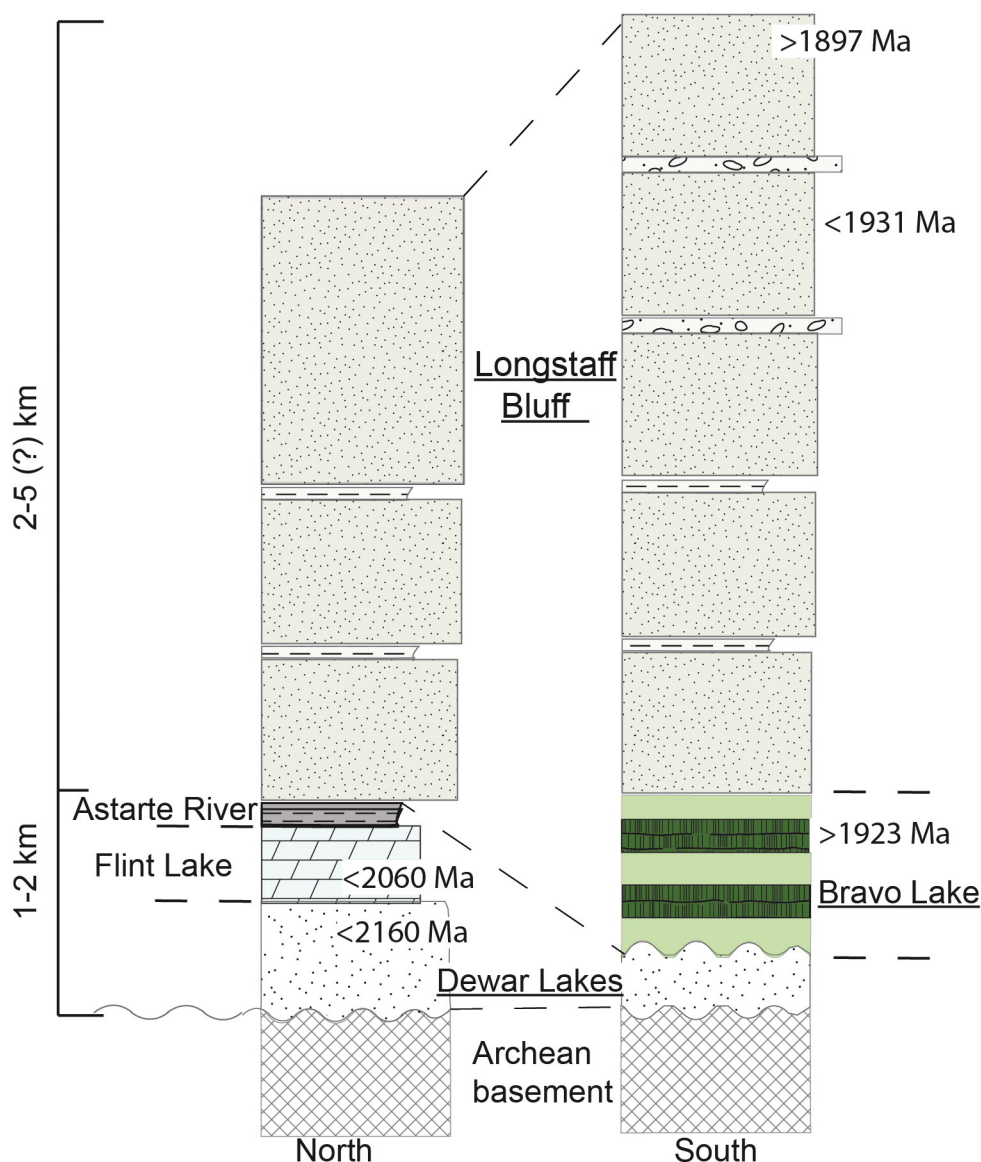


Fig. 2. Stratigraphic column of the Piling Group, showing how it differs from northern exposures (left) to southern exposures (right) on central Baffin Island (U/C = unconformity) with available age constraints (see Section 2 for geochronological data).

If pyrrhotite is present, the Fe_{carb} will reflect at least a partial leaching from pyrrhotite (Reuschel et al., 2012a). If iron carbonates are absent (as determined by independent methods), the Fe_{carb} term should not be used to calculate the highly reactive iron pool (Fe_{HR}). Samples were then treated with a sodium dithionite solution to extract iron associated with iron oxides (Fe_{ox}) that are reactive with hydrogen sulfide during early diagenesis. Magnetite (Fe_{mag}) was then extracted with an ammonium oxalate solution. Sequential extracts were analyzed on an Agilent 7500ce ICP-MS after 100-fold dilution in trace-metal grade 2% HNO_3 at the University of California, Riverside. Total chromium volatile sulfur (CVS), i.e. reduced sulfur from all sulfide-bound sulfur, was extracted during a two-hour hot chromous chloride distillation followed by iodometric titration (Canfield et al., 1986). Both pyrite and pyrrhotite are present in the BLF (see below), but all sulfide present was assumed to be pyrite when calculating Fe speciation parameters. However, in this case, this will not alter interpretations of the iron speciation results (as discussed below). Iron contents from the Fe_{carb} extraction step should be interpreted with caution in the presence of pyrrhotite, and are excluded in the calculation of (Fe_{HR}) here, since iron from pyrrhotite

already accounted for in the Fe_{py} term (CVS extraction). The total amount of highly reactive iron is therefore $Fe_{HR} = Fe_{ox} + Fe_{mag} + Fe_{py}$.

3.4. Major and trace element analyses

Total organic carbon (TOC) and total sulfur were determined using an Eltra Elemental Analyzer (EA). TOC was calculated as the difference between total carbon (determined by combustion) and total inorganic carbon (determined by acidification). Reproducibility was typically better than 0.1%. Powdered samples were analyzed by ACME Labs (Vancouver) via lithium tetraborate fusion and nitric acid digestion prior to analysis by ICP-OES (optical emission spectroscopy) for major elements and ICP (quadrupole) mass-spectrometry for trace elements. Analysis includes major elements (e.g., Fe_2O_3 , Al_2O_3) where detection limits were better than 0.01% and trace elements (e.g., Mo, Cr, V) where detection limits were typically better than 1 ppm. Quantitative wavelength-dispersive chemical analyses were done using the JEOL JXA-8530F electron microprobe at Yale University. We used a beam diameter of 1 μm and a beam current of 15 nA. In house natural and synthetic sulfide

Table 1
Geochemical data from the Bravo Lake Formation ORM samples analyzed in this study.

	PIL-1	PIL-2	PIL-3	PIL-4	PIL-5	PIL-6	PIL-7	PIL-8	PIL-9	PIL-10	PIL-11	PIL-12	PIL-13	PIL-14
Depth (m)	115.065	115.15	116.255	117.27	117.275	118.3	118.325	119.335	119.34	120.365	120.43	121.61	121.635	122.65
Mo (ppm)	25.6	37.1	51.3	24.8	18.2	23.5	24.2	23.0	31.2	17.4	17.7	12.8	19.9	22.5
U (ppm)	6.7	8.5	11.5	6.7	7.5	6.7	7.3	6.8	10.1	6.9	9.0	7.2	7.1	7.6
V (ppm)	314	387	565	286	296	244	239	272	251	264	343	255	352	336
Cu (ppm)	85	159	136	138	123	128	166	161	165	97	105	91	123	188
Ni (ppm)	255	247.8	250.7	212.5	173.6	175	201.9	232.5	242.8	121.8	133.7	124.6	178.2	260.9
Zn (ppm)	107	172	268	358	303	360	287	431	481	227	163	226	334	589
La (ppm)	15.9	37.3	41.4	37.1	34.4	36.3	36	33.6	36.5	33.9	38	32.2	39.1	32.9
Ce (ppm)	35.4	78.7	84.5	77.9	71.6	75.4	72.2	67.7	73.7	68.2	78.3	63.5	79.2	69.5
Pr (ppm)	4.04	9.14	10.02	8.85	8.34	8.61	8.54	8.05	8.85	7.98	8.92	7.54	9.25	7.93
Nd (ppm)	15.2	33.5	38.8	33.4	29.8	30.6	31.2	29.5	31.8	30.3	32.4	28.2	34.8	28.9
Sm (ppm)	2.87	5.77	6.82	5.78	5.36	5.55	5.73	5.58	5.58	5.19	5.72	5.2	5.65	5.33
Eu (ppm)	0.71	0.99	1.32	1.22	1.29	1.18	1.12	1.11	1.09	1.22	1.28	1.19	1.28	1.31
Gd (ppm)	2.69	4.73	5.7	5	4.36	4.69	5.01	5.46	4.6	4.31	4.84	4.71	4.55	5.03
Tb (ppm)	0.46	0.74	0.86	0.79	0.71	0.72	0.78	0.9	0.74	0.65	0.75	0.76	0.68	0.81
Dy (ppm)	2.64	4.04	4.69	4.25	3.85	3.75	4.18	5.38	4.1	3.54	3.98	4.47	3.82	4.61
Ho (ppm)	0.51	0.77	0.95	0.89	0.78	0.77	0.89	1.13	0.84	0.7	0.83	0.89	0.77	0.99
Er (ppm)	1.48	2.35	2.81	2.53	2.24	2.1	2.54	3.27	2.39	2.02	2.43	2.6	2.26	2.86
Tm (ppm)	0.25	0.37	0.42	0.41	0.35	0.34	0.39	0.47	0.38	0.31	0.39	0.4	0.35	0.42
Yb (ppm)	1.62	2.63	2.88	2.65	2.27	2.28	2.7	3.33	2.51	2.07	2.54	2.64	2.36	2.93
Lu (ppm)	0.27	0.41	0.45	0.39	0.36	0.34	0.41	0.51	0.38	0.33	0.4	0.42	0.38	0.44
Fe (wt.%)	9.20	8.69	8.97	7.70	6.04	6.58	7.59	8.76	8.09	4.93	5.32	4.80	6.15	9.51
Al (wt.%)	4.17	6.02	7.74	7.06	7.85	7.52	7.18	7.37	6.99	7.89	7.72	7.94	8.13	7.60
Mn (wt.%)	0.04	0.06	0.05	0.05	0.05	0.05	0.06	0.09	0.08	0.06	0.02	0.04	0.03	0.05
TOC (wt.%)	3.39	5.60	4.47	2.78	2.05	2.70	3.16	3.29	2.73	2.05	2.74	3.16	2.62	2.63
S (wt.%)	7.73	4.46	4.54	5.23	3.64	4.30	5.28	5.13	6.98	3.33	3.70	3.45	4.52	7.07
Fe _{HR} /Fe _T	0.68	0.60	0.61	0.59	0.64	0.63	0.59	0.58	0.64	0.60	0.76	0.66	0.60	0.58
Fe _{py} /Fe _{HR}	0.69	0.88	0.87	0.90	0.89	0.86	0.88	0.88	0.87	0.88	0.73	0.85	0.90	0.87
δ ³⁴ S (‰, VCDT)	−8.6	−9.0	−8.8	−9.9	−9.5	−9.9	−9.3	−9.2	−8.1	−9.2	−9.1	−9.1	−9.1	−9.8
δ ¹³ C _{org} (‰, VPDB)	−27.7	−27.6	−27.7	−27.8	−27.6	−27.6	−27.7	−27.6	−27.7	−27.7	−27.7	−27.5	−27.8	−27.6
δ ⁹⁸ Mo (‰), ±2σ	0.61 ± 0.09	0.56 ± 0.08	0.60 ± 0.09	0.62 ± 0.10	0.57 ± 0.09	0.55 ± 0.09	0.59 ± 0.08	0.60 ± 0.09	0.70 ± 0.09	0.68 ± 0.08	0.61 ± 0.11	0.7 ± 0.09	0.59 ± 0.09	0.67 ± 0.15

Table 2
Results of sequential iron extraction.

Sample ID	Depth (m)	Fe _{TOT} (wt.%)	Fe _{CARB} (wt.%)	Fe _{OX} (wt.%)	Fe _{MAG} (wt.%)	Fe _{PY} (wt.%)	Fe _{HR} (wt.%)	Fe _{HR} /Fe _T	Fe _{PY} /Fe _{HR}
PIL-1	115.065	9.20	5.85	0.08	1.9	4.31	6.3	0.68	0.69
PIL-2	115.15	8.69	0.29	0.17	0.5	4.62	5.3	0.60	0.88
PIL-3	116.255	8.97	0.22	0.06	0.6	4.77	5.5	0.61	0.87
PIL-4	117.27	7.70	1.02	0.13	0.3	4.08	4.5	0.59	0.90
PIL-5	117.275	6.04	0.38	0.13	0.3	3.42	3.9	0.64	0.89
PIL-6	118.3	6.58	1.47	0.30	0.3	3.56	4.1	0.63	0.86
PIL-7	118.325	7.59	0.83	–	0.3	3.95	4.3	0.59	0.88
PIL-8	119.335	8.76	0.16	–	0.4	4.50	4.9	0.58	0.88
PIL-9	119.34	8.09	0.15	0.25	0.4	4.50	5.2	0.64	0.87
PIL-10	120.365	4.93	0.15	0.14	0.2	2.61	3.0	0.60	0.88
PIL-11	120.43	5.32	0.51	0.48	0.6	2.94	4.0	0.76	0.73
PIL-12	121.61	4.80	0.06	0.22	0.3	2.68	3.2	0.66	0.85
PIL-13	121.635	6.15	0.05	0.10	0.3	3.31	3.7	0.60	0.90
PIL-14	122.65	9.51	0.13	0.37	0.4	4.79	5.5	0.58	0.87

standards were used for calibration and the sulfur interference on Mo was corrected. To optimize counting statistics, we used longer count times for Mo (750 s on peak). The total elemental composition for the sulfide phases ranged from 99% to 101%. Standard error of each element are reported in Table 3 and a review of analytical uncertainties are summarized in Ague and Eckert (2012).

3.5. Molybdenum isotope analysis

For Mo isotopes, powdered and ashed samples were processed using a three acid digestion, and a portion of this digest solution was doped with Mo double spike and passed through chromatographic columns. For all samples, a constant sample/spike ratio was maintained. We used a two-stage column for Mo separation procedure: a first stage

with an anion resin and a second stage of cation exchange separating Mo from remaining Fe. Blanks and duplicates were run in each set of columns. Molybdenum isotope compositions were analyzed using a Thermo NeptunePlus MC-ICP-MS at the Yale Metal Geochemistry Center. We used a ⁹⁷Mo–¹⁰⁰Mo double spike solution prepared gravimetrically using metal powders from Oak Ridge Laboratory. Optimization of the double spike isotope composition gave ⁹⁵Mo/⁹⁸Mo, ⁹⁷Mo/⁹⁸Mo and ¹⁰⁰Mo/⁹⁸Mo isotope ratios of 0.278, 16.663 and 15.704, respectively. Data reduction was done using Matlab according to Siebert et al. (2001). The NeptunePlus was operated at low-resolution mode with an ApexIR desolvating nebulizer, and all Mo isotope masses were measured together with ⁹¹Zr and ⁹⁹Ru in order to monitor isobaric interferences. During each session we performed frequent measurements of our lab Mo standard (Mo SPEX lot 11-177Mo), NIST-3137,

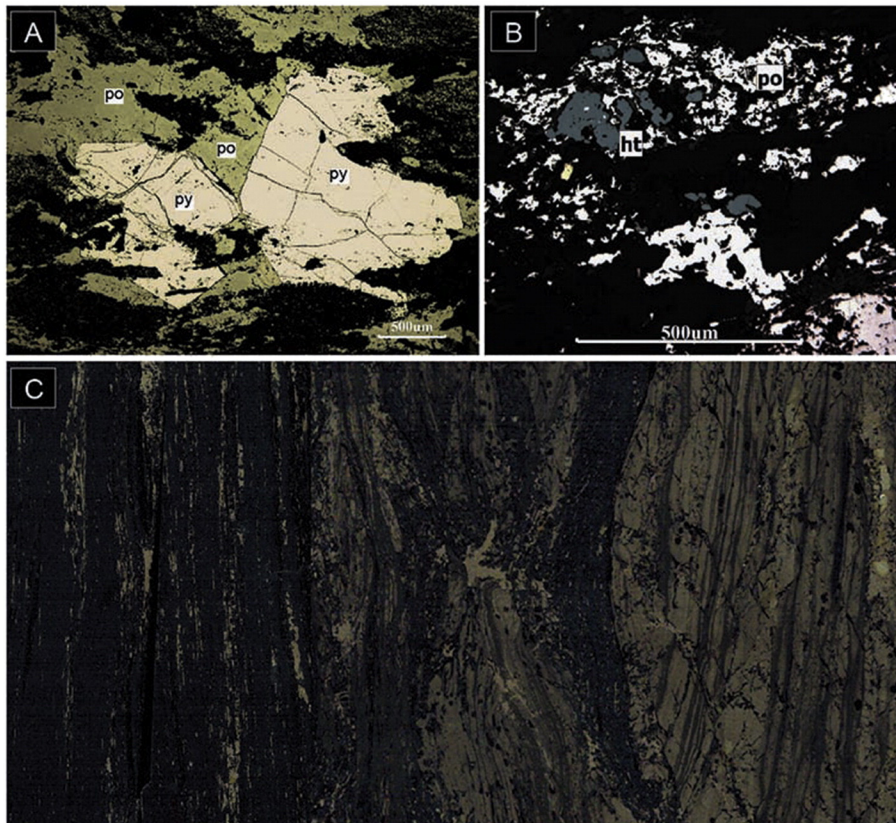


Fig. 3. Sulfide petrography of the Bravo Lake Formation. Reflected light microscopy shows pyrrhotite replacing pyrite (A) and pyrrhotite associated with hematite (B). Syndimentary/syngenetic sulfide laminae are preserved in ORM in drill core (C). The width of the core section is 4.5 cm.

Table 3
Chemical analysis of pyrite and pyrrhotite of the BLF.

Pyrite	Mg (wt.%)	Al (wt.%)	Si (wt.%)	Cr (wt.%)	Mn (wt.%)	Fe (wt.%)	Ni (wt.%)	Cu (wt.%)	P (wt.%)	S (wt.%)	V (wt.%)	Mo (wt.%)	Zn (wt.%)	Co (wt.%)	SUM (wt.%)
Point 1	0.0038	0	0.0008	0.00439	0	47.5601	0	0.0133	0.00431	53.507	0.00455	0.01083	0	0.1702	101.279
Point 2	0.0037	0.00147	0	0	0.00036	47.7646	0	0.02621	0	53.5919	0	0.00684	0	0.19032	101.585
Point 3	0.001	0	0	0.00092	0.01179	47.5266	0	0.0224	0.00251	53.4599	0.00201	0.0146	0.00135	0.14188	101.185
Point 4	0	0	0.0004	0	0	47.9069	0.0098	0.01724	0	53.4009	0.00103	0.01933	0	0.19825	101.554
Point 5	0.0026	0.00019	0.00092	0	0.00214	47.6507	0.0019	0.01699	0.0018	53.3073	0.00254	0.01847	0.003	0.22424	101.233
<i>Pyrrhotite-1</i>															
Point 1	0	0	0	0	0.00105	60.2442	0.0993	0.01711	0	39.1235	0.00323	0.05189	0.00101	0.0783	99.6195
Point 2	0.005	0.00048	0	0.00297	0.0021	61.1181	0.2087	0.0273	0	38.8672	0.00174	0.04877	0.00832	0.07166	100.362
Point 3	0	0	0.00139	0	0	60.3225	0.0378	0.01784	0.00539	39.331	0	0.0533	0	0.05074	99.8199
Point 4	0.0025	0	0	0.00392	0.03499	60.5769	0.0623	0.02028	0	39.3576	0	0.04963	0.01283	0.01655	100.138
<i>Pyrrhotite-2</i>															
Point 1	0	0	0	0	0	61.1743	0.201	0.01408	0.00302	38.5564	0	0.06415	0	0.09153	100.104
Point 2	0.0045	0	0	0	0	61.8298	0.2222	0.02803	0.00013	38.697	0	0.05037	0.00358	0.02315	100.859
Point 3	0.0019	0.00005	0.00249	0	0	61.6553	0.2003	0.03096	0	38.8952	0	0.05613	0.0051	0.075	100.922
Point 4	0	0	0	0	0	61.2357	0.1246	0.0368	0.001	39.3979	0	0.04886	0	0.01545	100.86
Point 5	0	0	0.00374	0.01236	0	61.3332	0.0923	0.03716	0.00151	39.452	0	0.04899	0.0039	0.06732	101.053

standard and Johnson Matthey Specpure® Mo plasma standard (Lot #802309E; also known as RochMo2) also used in previous studies, giving $\delta^{98/95}\text{Mo}_{\text{SPEX}} = \delta^{98/95}\text{Mo}_{\text{NIST3137}} - 0.37 \pm 0.06\%$ and $\delta^{98/95}\text{Mo}_{\text{SPEX}} = \delta^{98/95}\text{Mo}_{\text{RochMo2}} - 0.04 \pm 0.04\%$, respectively. The typical error on each measurement was 0.06‰ (2 σ). Error, based on duplicate samples and single column batch standards for this study, was <0.1‰. Molybdenum isotope composition is reported using the common δ notation, where $\delta^{98}\text{Mo}$ (‰) = $[(^{98}\text{Mo}/^{95}\text{Mo})_{\text{sample}} / (^{98}\text{Mo}/^{95}\text{Mo})_{\text{RochMo2}} - 1] \cdot 1000$.

4. Results

Geochemical results (major/trace element, isotopic, and Fe-speciation) are presented in Figs. 4–5 and Tables 1–2. Samples from the BLF show elevated total organic carbon (TOC) and total sulfur (TS) content, with TOC values up to 5.6 wt.% and TS values up to 7.7 wt.% and a range in TOC and TS values of 2.1 to 5.6 wt.% and 3.5 to 7.7 wt.%, respectively. S/C ratios range from 1.1 to 2.7 (average = 1.8). Both pyrite and pyrrhotite are present within the BLF (Fig. 3). These sulfide minerals are ubiquitous and occur as lenses, layers, and metamorphic replacements (pyrrhotite). Trace element abundances (e.g., Mo, U) and major element (e.g., Fe/Al) ratios are also elevated with respect to crustal levels, with a maximum concentration of 51 ppm for Mo, 11.5 ppm for U, 6.7 for U_{auth} (authigenic U is estimated as $U_{\text{auth}} = U - \text{Th}/3$), 565 ppm for V, and all Fe/Al ratios ≥ 0.6 . Ratios for Mo/U average 3.1 (max. = 4.5), and V/Mo ratios average 13.5 (max. = 19.9). The sulfur isotopes record moderately depleted $\delta^{34}\text{S}$ values, with an average value of -9.3% and a range of values from -8.3 to -10.0% . Results from organic carbon isotope analysis show a narrow range in $\delta^{13}\text{C}_{\text{org}}$ values (-28.5 to -28.8%). Values of $\delta^{98}\text{Mo}$ vary from 0.55 to 0.70‰, with an average $\delta^{98}\text{Mo}$ of $0.62 \pm 0.05\%$. The chemical composition of sulfide phases from electron microprobe analysis is shown in Table 3. Mo is elevated in pyrrhotite relative to pyrite and relatively invariant within individual sulfide grains.

5. Discussion

5.1. Sulfides in the BLF and possible effects from metamorphism

Given that pyrite in fine-grained metasedimentary rocks will undergo thermal decomposition to pyrrhotite above temperatures as low as 200 °C (Craig and Vokes, 1993), we first discuss sulfide mineral paragenesis to assess the potential impact on our paleoredox proxy results. Both pyrite and pyrrhotite are present in the BLF ORM and are typically blocky or euhedral. Pyrrhotite is sometimes associated with hematite in thin section, suggesting pyrrhotite growth potentially at the expense of

iron oxides (Fig. 3). Other hematite grains contain rhombic pyrrhotite inclusions or are overgrown by microcrystalline quartz. Pyrrhotite is overgrown locally by biotite, indicating pyrrhotite growth prior to retrograde metamorphism. Assuming the hematite is diagenetic and was stable at metamorphic P–T, thermal decomposition of pyrite reacted with iron from hematite to allow for pyrrhotite growth. Pyrite is assumed to be diagenetic, since pyrite in organic-rich sediments most commonly forms during diagenetic reactions between detrital iron minerals and H_2S (e.g., Raiswell, 1982). Pyrrhotite is not common as a sedimentary diagenetic mineral, but typically forms instead from the thermal decomposition of syngenetic or diagenetic pyrite during metamorphism (e.g., Ferry, 1981; Craig and Vokes, 1993).

The thermal breakdown of pyrite forms pyrrhotite by several different reactions, that either release sulfur that then reacts with iron from iron oxides (or iron silicates) existing in the rock, or, alternatively, with an external iron-bearing fluid (Ferry, 1981). In either reaction, the sulfur concentration in the system remains constant. In the absence of iron oxides/silicates or iron-rich fluids, pyrite decomposition in organic matter-rich sediments results in pyrrhotite growth, but also in a loss of sulfur (as H_2S) and CO_2 (Ferry, 1981). Although any of these reactions are possible given the composition and history of the BLF, petrographic evidence indicates an association of pyrrhotite growth within or around hematite, suggesting that some pyrrhotite formation might have occurred via the breakdown of pyrite and replacement of iron oxides (e.g., hematite). Despite this petrographic relationship, hematite is still ubiquitous in thin sections, suggesting that this transformation was far from complete. We argue that although some pyrite was converted to pyrrhotite during metamorphism, the sulfur content of the rock did not change significantly. Extremely large shifts in the content of sulfide iron in the examined ORMs would be needed to alter Fe proxy-based interpretations about depositional marine redox conditions (see below).

Our results report the $\delta^{34}\text{S}$ composition of all chromium-reducible sulfur (CRS) in the samples, therefore the isotopic composition of both pyrite and pyrrhotite are combined. Experimental and empirical data suggest that the $\delta^{34}\text{S}$ composition of pyrrhotite in organic matter-rich metapelites is very similar to that of the initial pyrite prior to sulfur liberation during metamorphic devolatilization (e.g., Ripley and Snyder, 2000; Luepke and Lyons, 2001; Alirezai and Cameron, 2001). Importantly, there is typically only a small fractionation (0.2 to 0.3‰) observed between pyrite and pyrrhotite formed during metamorphism in organic matter-rich metapelites (between 500 and 600 °C), as is relevant to our sample suite, and the isotopic differences between pyrite in low-grade or unmetamorphosed pelites and pyrrhotite in higher grade equivalent rocks is very small (e.g., Ferry, 1981; Yamamoto, 1984; Oliver et al., 1992; Ripley and Snyder, 2000). Although some studies have

reported large fractionations between pyrite and pyrrhotite, the reactions in these experiments were of a short duration (e.g., [Kajiwara et al., 1981](#)), whereas experiments that reached thermodynamic equilibrium better reflecting geologic time scales—or conducted under reducing conditions and observations in natural systems show very small fractionations (e.g., [Ripley and Snyder, 2000](#); [Luepke and Lyons, 2001](#); [Alirezaei and Cameron, 2001](#)). Thus, we conclude that sulfur isotope fractionation between pyrite and pyrrhotite is minimal and that the bulk sulfur content of our samples remained relatively constant during the thermal decomposition of pyrite.

Assuming a closed system with respect to total sulfur and iron contents, the Fe_{HR} term should remain unaffected, since it is still the sum of oxide, magnetite, pyrite, (and carbonate) iron partition fractions ($Fe_{HR} = Fe_{ox} + Fe_{mag} + Fe_{py} + Fe_{carb}$), even if some of these phases exchanged during metamorphic mineral transformations. Alternatively, if reactive iron mineral phases (e.g., oxides, carbonate) are transformed into poorly-reactive silicate phases, the effect might be a decrease in the Fe_{HR} term, leading to an overestimation of the Fe_{py}/Fe_{HR} values, while lowering Fe_{HR}/Fe_T values ([Reinhard et al., 2013a](#)). The transformation of pyrite to pyrrhotite during metamorphism might result in a loss of pyrite-bound sulfur (as discussed above). In this case, the Fe_{HR}/Fe_T term is predicted to be *underestimated* in both ferruginous and euxinic paleo-environments, whereas Fe_{py}/Fe_{HR} values are predicted to be similarly underestimated in ferruginous environments or experience no change at all in euxinic environments ([Reinhard et al., 2013a](#)). This relationship is anticipated even in a case where all CVS-extractable sulfur is assumed to be stoichiometric pyrite, as we have done here. Extractable iron from Fe_{carb} should be interpreted with caution, however, in the presence of pyrrhotite, since the sodium acetate extraction can leach some iron from monosulfides (cf. [Reuschel et al., 2012a](#)). If iron carbonates are absent, but pyrrhotite is present, Fe_{carb} should be excluded from the calculation of the highly reactive iron pool (Fe_{HR}) in order to avoid spurious Fe_{HR}/Fe_T ratios that could be artificially high and Fe_{py}/Fe_{HR} that could be artificially low. Bearing these considerations in mind, the possibility for potential assertions of false euxinia is unlikely in pyrite–pyrrhotite bearing ORMs (cf. [Lyons and Severmann, 2006](#); [Reinhard et al., 2013a](#)).

As a result of the thermal decomposition of pyrite into pyrrhotite, trace elements, including Mo, were transferred into pyrrhotite. This is marked by elevated Mo concentrations in pyrrhotite, relative to

adjacent pyrite ([Fig. 6](#)). This indicates that there was small-scale redistribution of Mo during metamorphism. Mo is typically hosted in the matrix of black shales, associated with the organic matter (e.g., [Chappaz et al., 2014](#)). During organic matter breakdown at elevated temperatures and pressures some Mo was remobilized, largely into the metamorphic pyrrhotite. Secondary incorporation into pyrrhotite likely prevented larger (meter) scale homogenization of Mo isotope signatures. Molybdenum incorporation into pyrrhotite likely allowed for large stratigraphic variations in Mo concentrations without significant correlation to total S contents. (see [Fig. 5](#))

5.2. Iron speciation

The iron speciation technique, when used with care, provides a powerful proxy that can help to determine paleo-redox state (oxic, ferruginous, or euxinic) during sediment deposition, and data obtained with this technique have greatly shaped our ideas of evolving Proterozoic oceanic redox state (e.g., [Poulton et al., 2004](#); [Poulton and Canfield, 2005](#); [Canfield et al., 2008](#); [Scott et al., 2008](#); [Poulton and Canfield, 2011](#); [Planavsky et al., 2011](#)). This technique has the potential to provide insight into the redox state of seawater during the deposition of the BLF. If the ratio of highly-reactive iron to total iron (Fe_{HR}/Fe_T) is greater than 0.38, the depositional environment is considered anoxic. Furthermore, if $Fe_{HR}/Fe_T > 0.38$ and the ratio of pyrite iron to highly-reactive iron (Fe_{py}/Fe_{HR}) is greater than ~0.7, the depositional environment is considered euxinic (see [Poulton and Canfield, 2011](#) and references therein). All samples from the BLF have Fe_{HR}/Fe_T ratios > 0.38 , and most of them have $Fe_{py}/Fe_{HR} \geq 0.7$, suggesting predominantly euxinic depositional conditions ([Figs. 4 and 5](#); [Table 2](#)). The lowermost sample plots near the margin of the euxinic-ferruginous field of a Fe_{HR}/Fe_T vs. Fe_{py}/Fe_{HR} plot ([Fig. 4](#)), with a Fe_{py}/Fe_{HR} of 0.69. With an outlier at the base of the section, it is not clear if this trend is capturing fluctuating redox state during a transition from ferruginous to euxinic conditions. Either way, the BLF shows Fe_{py}/Fe_{HR} ratios indicative of dominantly euxinic water column conditions ([Fig. 4](#)).

We can be confident that the Fe_{HR}/Fe_T ratios are truly indicative of anoxic depositional conditions, even in the presence of pyrrhotite ([Section 5.1](#)). Although some pyrrhotite has overgrown hematite, the presence of ubiquitous hematite still preserved in thin section suggests

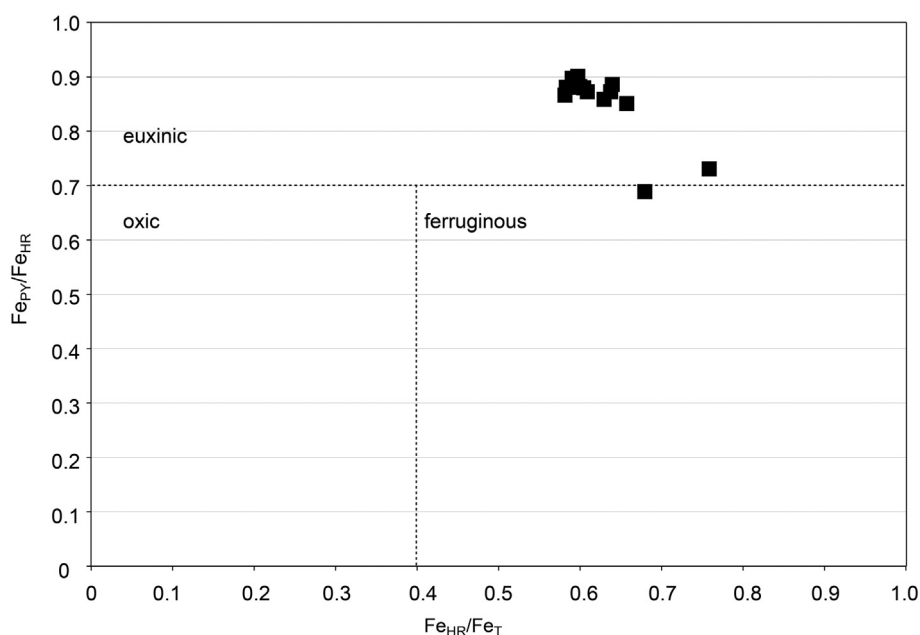


Fig. 4. Plot of Fe_{HR}/Fe_T vs. Fe_{py}/Fe_{HR} results for the Bravo Lake Formation, showing dominantly euxinic bottom water conditions.

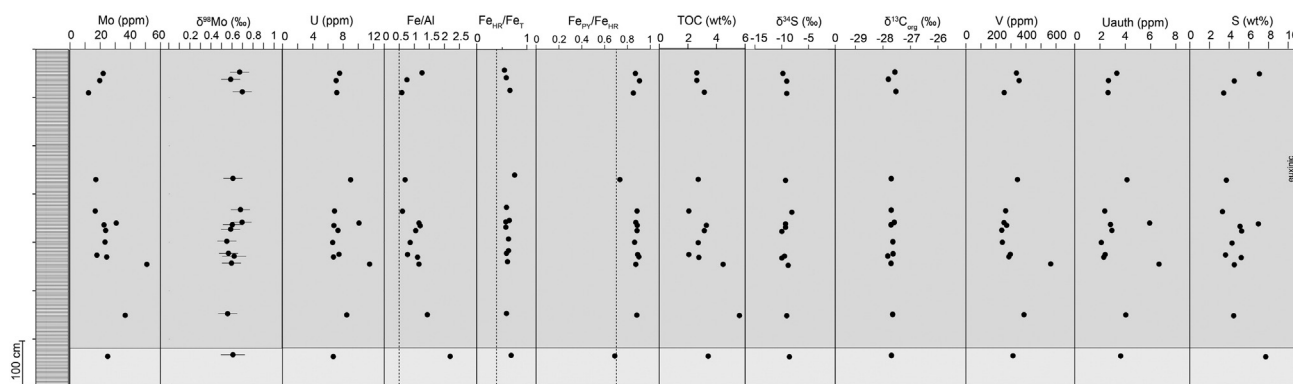


Fig. 5. Stratigraphic variations in trace and major element concentrations and isotope values in the Bravo Lake Formation delineating environmental conditions.

that this reaction did not go to completion, and therefore did not appreciably decrease Fe_{HR} values. Additionally, theoretical predictions for ORMs that experienced some pyrite–pyrrhotite transition (Reinhard et al., 2013a) infer that Fe_{py}/Fe_{HR} values would either be underestimated or remain the same, which also validates our interpretation of euxinia from Fe_{py}/Fe_{HR} values that are ≥ 0.7 and dominantly > 0.8 .

5.3. Sulfur isotopes

The sulfur isotope record from the BLF is consistent with euxinic conditions. The sulfur records moderately depleted $\delta^{34}S$ values (-10 to -8.3% ; Fig. 5), which fall within the wide range of observed values in post-GOE sedimentary sulfides (e.g., Canfield, 2001). Post-GOE $\delta^{34}S$ sulfide values are interpreted to reflect bacterial sulfate reduction, since the maximum fractionations are of the same magnitude as those observed for modern sulfate reducers under non-limiting sulfate concentrations (e.g., Canfield, 2001). An epigenetic hydrothermal origin is unlikely for S isotope values of the BLF sulfides, since their $\delta^{34}S$ values do not approach zero (e.g., Loukola-Ruskeeniemi, 1991). Instead, their depleted $\delta^{34}S$ values are most consistent with dissimilatory sulfate reduction (Canfield, 2001), perhaps at non-limiting levels of sulfate, though this would need to be confirmed with coeval $\delta^{34}S_{sulfate}$ values. Previous determinations of ~ 2.1 Ga seawater sulfate sulfur isotope composition range from 10‰ to 21‰ (Schröder et al., 2008; Guo et al., 2009; Reuschel et al., 2012b), suggesting a fractionation between sulfide and seawater sulfate around 19‰ to 30‰; this remains the best approximation available for BLF-time (ca. 1.93 Ga). These fractionations—which are appreciable for Proterozoic shales (see Scott et al., 2014)—might

be consistent with a scenario of euxinic conditions where sulfate reduction and pyrite formation are occurring in the water column instead of in porewaters, where closed system behavior is likely.

5.4. C_{org} isotopes and S/C ratios

The $\delta^{13}C_{org}$ values (average -27.7%) are typical marine organic matter values. Metamorphism, causing devolatilization of the organic matter fraction would result in more positive $\delta^{13}C_{org}$ values due to preferential loss of CO_2 with the lighter isotope (Schidlowski, 2001). Some devolatilization is expected, as the BLF rocks underwent metamorphism (400 to 500°C in the study area); therefore, the $\delta^{13}C_{org}$ values reported here are likely to be more enriched in ^{13}C relative to their depositional values due to Rayleigh distillation (e.g., Valley, 1986). However, the presence of marine signatures suggests relatively minor C loss. The S/C ratios in the BLF (average 1.8) are consistent with early Paleozoic normal marine sediments (2; Raiswell and Berner, 1986). This supports our assertion that the BLF represents a marine succession and was probably influenced by a marine biomass that produced organic matter content and associated light C isotope values.

5.5. Trace elements

The concentration of redox-sensitive trace metals (e.g., Mo, U, and V) in marine sediments provides insight into both local depositional conditions and global oceanic redox state, since their burial rate is much higher under anoxic water columns relative to oxic water columns, and the magnitude of enrichment above crustal levels mirrors the size of the oceanic reservoir of those elements (e.g., Emerson and Huested, 1991). Recent studies have shown that the concentration of redox-sensitive elements in seawater reflects the evolving redox state of the atmosphere–ocean system and its impact on the marine metal inventory and is highest in well-oxygenated oceans with spatially limited water column anoxia or euxinia (e.g., Scott et al., 2008; Partin et al., 2013; Reinhard et al., 2013b). The enrichment of Mo, U, V, and Fe/Al above crustal levels in the BLF ORM is consistent with deposition under an anoxic water column (Figs. 4, 5). Molybdenum and V concentrations ($Mo_{avg} = 25$ ppm; $V_{avg} = 315$ ppm), for example, are moderate and expected for this time period (cf. Scott et al., 2008; Sahoo et al., 2012). Mo concentrations in the BLF are typical of sediments deposited in modern restricted anoxic basins such as Saanich Inlet, Namibian Shelf, and the Black Sea (Algeo and Lyons, 2006). Both the average concentrations for Mo (25 ppm) and Mo normalized to TOC ($Mo/TOC_{avg} = 8.1$ ppm/wt.%) in the BLF are remarkably similar to average values reported in Scott et al. (2008) for anoxic Proterozoic (2000 to 550 Ma) black shales ($Mo_{avg} = 24$ ppm, $Mo/TOC_{avg} = 6.4$ ppm/wt.%). It should be noted that Mo/TOC ratios in the BLF might be overestimated, or the Mo/TOC slope steepened, given that some organic matter content would be lost through volatilization during catagenesis and

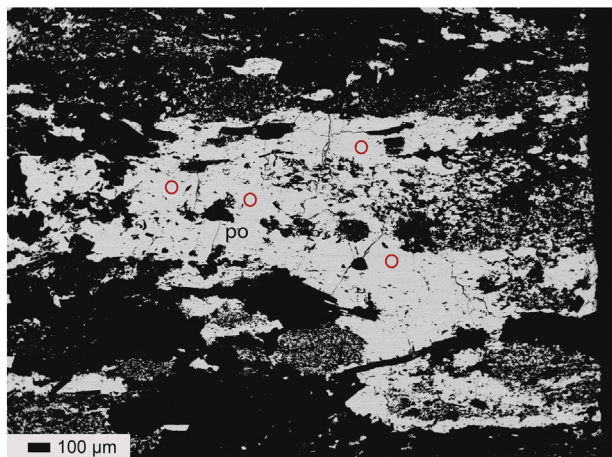


Fig. 6. Mo spots on pyrrhotite from electron microprobe analysis. Average Mo concentration = 537 ppm.

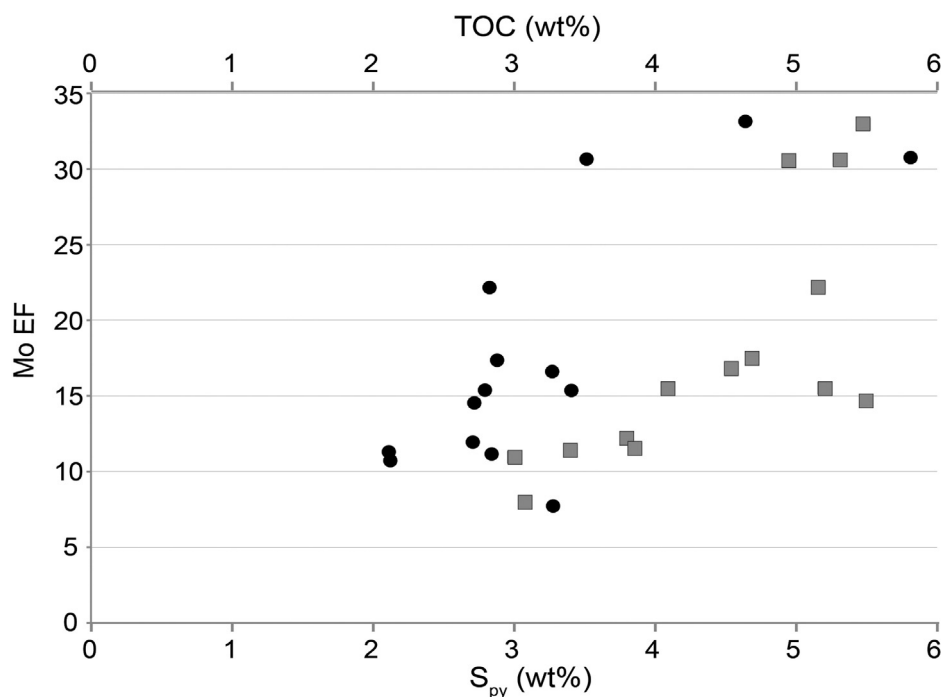


Fig. 7. Crossplot of Mo vs. TOC and Mo vs. S_{py} . Mo contents are presented as an “enrichment factor,” where $MoEF = (Mo/Al)_{sample}/(Mo/Al)_{crust}$. Black circles represent Mo-TOC values; grey squares represent Mo- S_{py} values. Crust values from Taylor and McLennan (1985).

metamorphism. Nevertheless, the BLF maintained relatively high TOC (2 to 5.6 wt.%) and retained typical organic matter carbon isotope signatures, suggesting relatively minor C loss. Given the broad positive covariation of Mo and TOC values (Fig. 7), some Mo was likely scavenged by complexation with organic matter particles, which have been shown to covalently bond to molybdates (Tribouillard et al., 2006). Mo content shows a stronger correlation with S_{py} content than with TOC (Fig. 7), implying that sulfidity probably had a stronger control over Mo fixation than did organic matter content; a similar relationship is seen in Black Sea sediments (Neubert et al., 2008). The covariation of Mo with S_{py} and more weakly, but still positively, with TOC, as well as the lack of molybdenite or other hydrothermal Mo minerals, suggests that Mo content was not likely enhanced by secondary enrichment processes. Vanadium and U concentrations are less well correlated with TOC, but this is typical for euxinic environments, since these elements tend to be associated with authigenic mineral phases rather than the organic fraction in euxinic depositional environments (e.g., Tribouillard et al., 2006).

The difference in Mo enrichments between Phanerozoic and Proterozoic euxinic shales is one of the key lines of evidence for more widespread anoxia in the Proterozoic (e.g., Scott et al., 2008; Lyons et al., 2014). However, this conclusion was previously based on only six euxinic Proterozoic successions (Scott et al., 2008; Reinhard et al., 2013b). Therefore, the recognition of another Proterozoic organic-rich euxinic succession with lower-than-Phanerozoic Mo enrichments is noteworthy. Further, there are lower concentrations of U and Mo in the BLF compared to euxinic shales deposited during GOE-Lomagundi interval (cf. Scott et al., 2008; Partin et al., 2013). This trend to lower enrichments of redox-sensitive elements was previously interpreted as reflecting a decrease in oxygen level in the atmosphere–ocean system following the Lomagundi Event (e.g., Partin et al., 2013).

A reservoir effect might be expected to affect redox-sensitive trace element ratios and profiles (e.g., Mo, U, V) if the Piling basin was restricted from the open ocean. However, local reservoir drawdown is inconsistent with high V concentrations—relative to modern anoxic sediments—and does not explain the high V/Mo ratios, given that the residence time of Mo is likely to be longer than V, as is the case in the modern ocean (e.g., Emerson and Huested, 1991).

Elevated concentrations of base metals (such as Cu, Zn, Ni, Hg, and Mn) might be expected if there was an addition of these elements via epigenetic hydrothermal fluids. However, Mn concentrations are not elevated ($Mn < 0.08\%$) and neither are Hg concentrations (0.01 ppm). Base metals such as Cu, Zn, and Ni also have near-crustal values (Table 1) and are strongly depleted, for example, relative to the broadly coeval base-metal enriched Talvivaara black schists in Finland (Loukola-Ruskeeniemi, 1991). Additionally, in a spider diagram of rare earth elements (REEs) normalized to chondrite (Fig. 8), BLF samples show a negative Eu anomaly, which also argues against the influence of hydrothermal fluids (e.g., German et al., 1990; Bau, 1991).

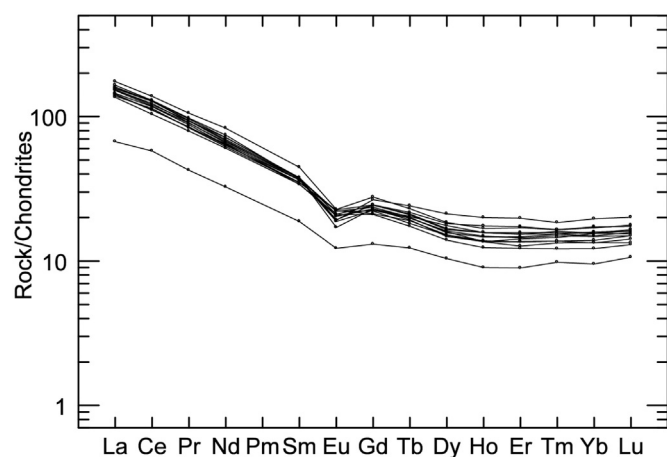


Fig. 8. REE diagram of BLF shale showing negative Eu anomaly, normalized to chondrite (Sun and McDonough, 1989).

5.6. Mo isotopes

The seawater Mo isotope composition is controlled by the extent of Mo burial in oxic, suboxic, and euxinic conditions. Oxidic and suboxic

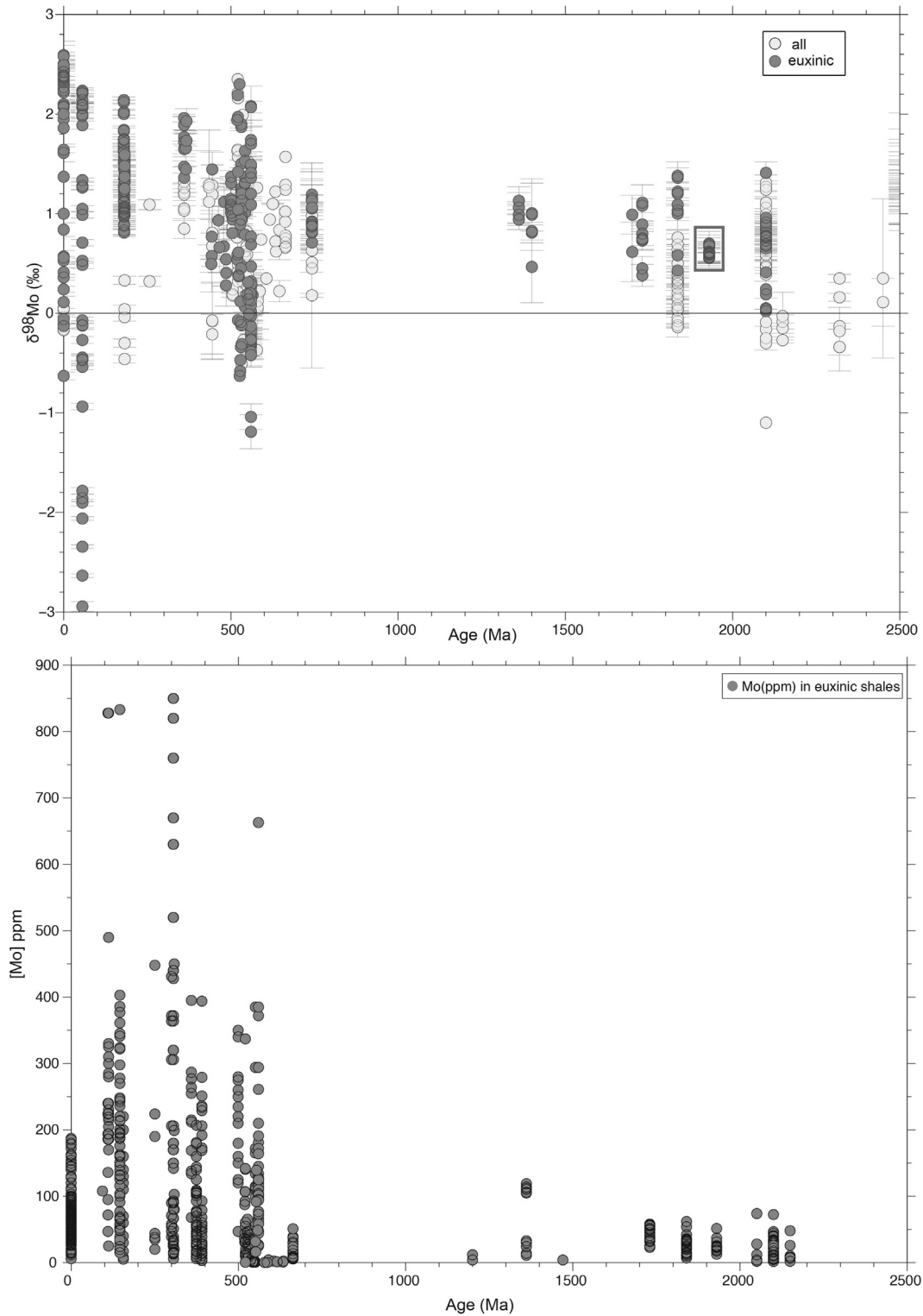


Fig. 9. Compilation of Mo isotopes ($\pm 2\sigma$ error bars plotted) and [Mo] from organic-rich mudrocks (ORMs) through time (see Supplementary materials for references of compiled $\delta^{98}\text{Mo}$ data (n = 790); [Mo] database (n = 857) modified from Reinhard et al., 2013b). $\delta^{98}\text{Mo}$ data from the BLF is highlighted in the box.

environments preferentially bury light Mo, which drives the dissolved seawater Mo isotope value heavy (Barling et al., 2001; Siebert et al., 2003; Arnold et al., 2004). In contrast, it is typically thought that there is more limited fractionation during Mo burial in euxinic environments (Barling et al., 2001; Arnold et al., 2004). In this framework, seawater Mo isotope values can be used to estimate the extent of euxinic environments on a global scale, and euxinic shales can come close to capturing

seawater values (Arnold et al., 2004). Accordingly, heavy Mo isotope values in euxinic shales have been used as evidence for relatively limited euxinia (as we see today), and light values, those near the composition of the crust, have been used as evidence for widespread euxinia (e.g., Poulson et al., 2006; Pearce et al., 2008; Kendall et al., 2011). There are, however, a few complications to this story. Foremost, since this framework was proposed (Arnold et al., 2004) it has become clear that

euxinic shales do not always capture seawater values (e.g., Noordmann et al., 2015). Data from the Black Sea shows that aqueous H_2S concentrations are also critical, as this must reach a critical threshold for thiomolybdate to dominate over molybdate. Black Sea sediments deposited under shallower water (<400 m) conditions, though still euxinic, have $\delta^{98}\text{Mo}$ values that are depleted with respect to sediments below the critical threshold H_2S concentration that allows complete Mo fixation (Neubert et al., 2008). This observation demands refinements to the global isotope mass balance, but most importantly, it means that care must be taken when interpreting Mo isotope data from euxinic shales, which might reflect a range of sulfidities and partial Mo removal, resulting in variable $\delta^{98}\text{Mo}$ fractionations.

Nevertheless, a case can be made that the BLF ORM likely captures at least a minimum estimate for coeval seawater $\delta^{98}\text{Mo}$ composition at ~0.7‰. Foremost, there is remarkably little variability in the BLF ORM Mo isotope values, despite strong variability in the Mo enrichments (Fig. 5). This observation contrasts with modern anoxic and sulfidic settings where there are fractionations from seawater. For instance, Baltic Deep cores display large (>1‰) variability on a cm scale (Noordmann et al., 2015). Variability in Black Sea sediment $\delta^{98}\text{Mo}$ composition is associated with variable water column sulfide content (Neubert et al., 2008). The BLF values are similar to the average composition of riverine waters, a major flux of Mo to the oceans (Archer and Vance, 2008), which could be used to suggest that Mo burial was dominated by euxinic environments. Recent investigations suggest, however, a relatively heterogeneous Mo isotopic composition for continental crust, with an average value of about 0.4‰ (Greber et al., 2014; Voegelin et al., 2014), which might be a more representative estimate for the Mo isotopic composition of continental runoff. There are some remaining uncertainties in the Mo isotope mass balance, but it is clear that oxic conditions must have been extremely limited to have a Mo isotope value that approaches the estimated modern average riverine value of +0.7‰ (Archer and Vance, 2008). However, it is possible that the Mo isotope composition of the crust has gotten progressively heavier with time due to subduction of isotopically light Mo in an oxic ocean (Planavsky and Reinhard, 2014). However, this change should be minimal and the input flux in the Paleoproterozoic at minimum should be close to igneous input values, near 0.4‰. It is unclear how the Mo isotopic composition of riverine waters has evolved through time given the possibility for variations in weathering intensity or Mo isotope composition of crustal materials, especially of isotopically-heavy organic-rich shale deposited in largely oxic oceans (cf. Archer and Vance, 2008).

The BLF is bracketed by maximum $\delta^{98}\text{Mo}$ values of ~1.4‰ in euxinic shales at 1.85 Ga and 2.1 Ga (Fig. 9). The lower $\delta^{98}\text{Mo}$ values in the BLF could be attributed to 1) static seawater $\delta^{98}\text{Mo}$ composition between 2.1 and 1.85 Ga, but incomplete Mo fixation within only a weakly sulfidic water column, resulting in lower-than-seawater $\delta^{98}\text{Mo}$ values, 2) seawater at ~1.93 Ga had a lower $\delta^{98}\text{Mo}$ composition reflecting a greater spatial extent of ocean euxinia relative to 2.1 and 1.85 Ga, or 3) post-depositional homogenization processes (such as volatilization or mixing with fluids during regional metamorphism; cf. Greber et al., 2014) that altered primary sedimentary $\delta^{98}\text{Mo}$ values. Since the effect of regional metamorphism on sedimentary $\delta^{98}\text{Mo}$ values is unknown, we can only speculate that if the $\delta^{98}\text{Mo}$ values in the BLF were altered, they would be driven to lighter, more crustal-like values. Therefore, taking into account any of the above possibilities, the conservative view suggests that the maximum $\delta^{98}\text{Mo}$ values from the BLF of 0.7‰ represent at least a *minimum* estimate for coeval seawater. Obtaining Mo isotopic data from other ORMs of this age would further constrain a seawater signature for this time, as would future studies that systematically document the effect of regional metamorphic facies variation on sedimentary $\delta^{98}\text{Mo}$ composition. Further, more Proterozoic data are needed so that a statistically-based approach might be possible. The BLF ORM data will help move us in that direction, as the Proterozoic Mo isotopic record is currently relatively sparse (Fig. 9).

5.7. Oceanic redox conditions during the ca. 2.06 to 1.88 Ga time interval

The traditional view of Earth's oxygenation assumes a unidirectional increase in oxygen content of the atmosphere and oceans since the GOE (Holland, 1984; Kump, 2008). Alternative models have proposed changes in the redox state of the ocean in the mid-Proterozoic (1.8 to 0.8 Ga) beginning with the cessation of banded iron formation deposition after ~1.85 Ga, when the oceans might have transitioned to euxinic (Canfield, 1998), suboxic (Slack et al., 2007), or oxic conditions (Holland, 1984); the latter of which is no longer widely accepted. The euxinic model postulates that ferruginous oceans became euxinic at ~1.8 Ga, as sulfate levels in the ocean increased via enhanced oxidative continental weathering (Canfield, 1998). The “Canfield ocean” model also provides a mechanism for the disappearance of iron formations at this time, as available iron was titrated to pyrite in the presence of sulfide. Euxinic depositional conditions are documented at ~1.85 Ga (Poulton et al., 2004, 2010), though euxinia was spatially- and temporally-restricted thereafter (Shen et al., 2003; Kendall et al., 2009; Reinhard et al., 2013b). Long-lived and pervasive euxinia in the mid-Proterozoic oceans is not likely to be tenable due to mass balance considerations of Mo concentrations in mid-Proterozoic shales (Reinhard et al., 2013b). Additionally, several temporally and geographically separated basins show deposition under ferruginous conditions (Planavsky et al., 2011), and still other, deep-water strata show evidence for suboxic deposition (Slack et al., 2007). These data demonstrate that ideas of long-lived and homogenous oceanic redox state in the mid-Proterozoic oceans are likely oversimplified.

Another model to explain the brief reappearance of iron formations at ~1.9 Ga suggests that an enhanced iron flux sourced from hydrothermal vent fluids promoted iron mineral precipitation even in shallow waters, resulting in the return of giant iron formation deposits at this time (Bekker et al., 2010). In deeper water settings, an enhanced hydrothermal iron flux would accompany an enhanced flux of reductants, maintaining anoxic and ferruginous conditions, even if higher levels of sulfate were present. This increased hydrothermal activity has been linked to a mantle plume event at ca. 1.88 Ga (Bekker et al., 2010; Rasmussen et al., 2012). Hydrothermal fluxes, submarine volcanism, and mantle plumes might have a first-order control on basin-scale to global ocean anoxia (Condie et al., 2001; Bekker et al., 2010). The amalgamation of the supercontinent, Nuna, might be implicated in ~1.9 to 1.8 Ga events that influenced Earth's fledgling surface oxygen conditions.

There is evidence from Fe-speciation data and sulfur isotopes that euxinia was a pervasive, but likely spatially-limited, oceanic redox state during the Lomagundi Event (Scott et al., 2008; Planavsky et al., 2012; Scott et al., 2014). This would be expected if there were higher levels of oceanic sulfate associated with increased atmospheric oxygen during the Lomagundi Event. After the Lomagundi Event, oceanic redox conditions might have returned to a dominantly ferruginous state, under lower oxygen conditions. Ferruginous conditions are demonstrated by granular iron formation deposition at ~1.88 Ga, and it is proposed that ferruginous conditions dominated from ~1.93 to 1.88 Ga (Bekker et al., 2010). ORMs of the Bravo Lake Formation allow us to view a window into understanding the redox setting of seawater at this time. Stated more broadly, Bravo Lake Formation ORMs are post-Lomagundi Event and pre-loss of iron formations, so the BLF captures this transitional interval.

Our data from the ca. 1.93 Ga BLF demonstrates that, to the contrary, euxinic depositional conditions developed prior to the deposition of granular iron formations at ca. 1.88 Ga. Mounting evidence suggests that the oceans transitioned to a lower oceanic and atmospheric oxygen levels between ca. 2.06 and 1.88 Ga (e.g., Bekker and Holland, 2012; Partin et al., 2013; Lyons et al., 2014). A shift towards lower oxygen conditions should be accompanied by a global increase in pyrite burial, since the re-oxidation of sulfide would decrease as marine anoxia becomes more expansive (e.g., Canfield, 1998). Importantly, an increase

in pyrite formation would be in part from the weathering of sulfate evaporites deposited during the Lomagundi Event. The subsequent burial of this pyrite should result in a net increase of the oxidation state of the atmosphere–ocean system. The feedback between variable pyrite and organic matter burial and oxygen production predicts dynamic, rather than stable, atmospheric oxygen throughout the mid-Paleoproterozoic Era.

6. Conclusions

We document euxinic depositional conditions in ORM of the BLF, providing a much needed window into the composition of seawater in a shallow shelf environment at ca. 1.93 Ga. We conclude that euxinic conditions were widespread in the shallow ocean prior to and after the deposition of granular iron formations at ca. 1.88 Ga, in contrast to predictions of ferruginous conditions being the prevailing oceanic redox state for this time interval. Our study contributes new data for iron speciation; major and trace elements; and sulfur, organic carbon, and Mo isotopes from ca. 1.93 Ga greenschist-facies ORM to fill in the existing gap between the end of the Lomagundi Event (ca. 2.06 Ga) and the return of iron formation deposition at ca. 1.88 Ga. Specifically, anoxic conditions are indicated by parameters such as Fe_T/Al and Fe_{HR}/Fe_T ratios, and supported by elevated TOC and U, V, and Mo concentrations. Euxinic conditions are inferred from the ratio of Fe_{py}/Fe_T , Mo concentrations, and Mo and S isotopes. Future work should focus on testing the possibility of spatially and temporally variable redox architecture in the oceans in this interval (<2.06 to >1.88 Ga), as seen in the geologic record at 1.85 Ga, when contemporaneous ferruginous and sulfidic conditions were recorded in a basin transect (Poulton et al., 2010). Importantly, our study contributes to ongoing efforts to understand the redox evolution and architecture of Proterozoic oceans that might have stalled eukaryotic evolution (e.g., Lyons et al., 2014; Planavsky et al., 2014).

Acknowledgments

The authors acknowledge David Corrigan (GSC) and Commander Resources, GeoVector, and the AngloGold Baffin project for providing drill core samples. Funding and support were provided by the Geological Survey of Canada's Geo-mapping for Energy and Minerals (GEM) Program (C.A.P.). Funds were also provided by the NSERC Discovery and Accelerator grants (A.B.) and the U.S. NSF FESD Program and NASA Astrobiology (T.W.L.). M. Yun (University of Manitoba), S. Bates (UC, Riverside), and T. Tang and D. Asael (Yale) are gratefully acknowledged for their analytical assistance. Reviewers are thanked for their helpful comments.

Appendix A. Supplementary data

Supplementary data to this article can be found online at <http://dx.doi.org/10.1016/j.chemgeo.2015.09.004>.

References

Ague, J.J., Eckert, J.O., 2012. Precipitation of rutile and ilmenite needles in garnet: implications for extreme metamorphic conditions in the Acadian Orogen, U.S.A. *Am. Mineral.* 97, 840–855. <http://dx.doi.org/10.2138/am.2012.4015>.

Algeo, T.J., Lyons, T.W., 2006. Mo–total organic carbon covariation in modern anoxic marine environments: implications for analysis of paleoredox and paleohydrographic conditions. *Paleoceanography* 21, PA1016. <http://dx.doi.org/10.1029/2004PA001112>.

Alirezai, S., Cameron, E.M., 2001. Variations of sulfur isotopes in metamorphic rocks from Bamble Sector, southern Norway: a laser probe study. *Chem. Geol.* 181, 23–45. [http://dx.doi.org/10.1016/S0009-2541\(01\)00266-2](http://dx.doi.org/10.1016/S0009-2541(01)00266-2).

Archer, C., Vance, D., 2008. The isotopic signature of the global riverine molybdenum flux and anoxia in the ancient oceans. *Nat. Geosci.* 1, 597–600. <http://dx.doi.org/10.1038/ngeo282>.

Arnold, G.L., Anbar, A.D., Barling, J., Lyons, T.W., 2004. molybdenum isotope evidence for widespread anoxia in mid-Proterozoic oceans. *Science* 304, 87–90. <http://dx.doi.org/10.1126/science.1091785>.

Aspler, L.B., Chiarenzelli, J.R., Cousens, B.L., McNicoll, V.J., Davis, W.J., 2001. Paleoproterozoic intracratonic basin processes, from breakup of Kenorland to assembly of Laurentia: Hurwitz Basin, Nunavut, Canada. *Sediment. Geol.* 141–142, 287–318. [http://dx.doi.org/10.1016/S0037-0738\(01\)00080-X](http://dx.doi.org/10.1016/S0037-0738(01)00080-X).

Barling, J., Arnold, G., Anbar, A., 2001. Natural mass-dependent variations in the isotopic composition of molybdenum. *Earth Planet. Sci. Lett.* 193, 447–457. [http://dx.doi.org/10.1016/S0012-821X\(01\)00514-3](http://dx.doi.org/10.1016/S0012-821X(01)00514-3).

Bau, M., 1991. Rare-earth element mobility during hydrothermal and metamorphic fluid–rock interaction and the significance of the oxidation state of europium. *Chem. Geol.* 93, 219–230. [http://dx.doi.org/10.1016/0009-2541\(91\)90115-8](http://dx.doi.org/10.1016/0009-2541(91)90115-8).

Bekker, A., Holland, H.D., 2012. Oxygen overshoot and recovery during the early Paleoproterozoic. *Earth Planet. Sci. Lett.* 317–318, 295–304. <http://dx.doi.org/10.1016/j.epsl.2011.12.012>.

Bekker, A., Holland, H.D., Wang, P.L., Rumble, D., Stein, H.J., Hannah, J.L., Coetzee, L.L., Beukes, N.J., 2004. Dating the rise of atmospheric oxygen. *Nature* 427, 117–120.

Bekker, A., Kaufman, A.J., Karhu, J.A., Beukes, N.J., Swart, Q.D., Coetzee, L.L., Eriksson, K.A., 2001. Chemostratigraphy of the Paleoproterozoic Duitschland Formation, South Africa: implications for coupled climate change and carbon cycling. *Am. J. Sci.* 301, 261–285. <http://dx.doi.org/10.2475/ajs.301.3.261>.

Bekker, A., Slack, J., Planavsky, N., Krapež, B., Hofmann, A., Konhauser, K.O., Rouxel, O.J., 2010. Iron formation: the sedimentary product of a complex interplay among mantle, tectonic, oceanic, and biospheric processes. *Econ. Geol.* 105, 467–508.

Canfield, D.E., 1998. A new model for Proterozoic ocean chemistry. *Nature* 396, 450–453.

Canfield, D.E., 2001. Biogeochemistry of sulfur isotopes. *Rev. Mineral. Geochem.* 43, 607–636. <http://dx.doi.org/10.2138/gsrmg.43.1.607>.

Canfield, D.E., 2005. The early history of atmospheric oxygen: homage to Robert A. Garrels. *Annu. Rev. Earth Planet. Sci.* 33, 1–36.

Canfield, D.E., Farquhar, J., Zerkle, A.L., 2010. High isotope fractionations during sulfate reduction in a low-sulfate euxinic ocean analog. *Geology* 38, 415–418. <http://dx.doi.org/10.1130/G30723.1>.

Canfield, D.E., Ngombi-Pemba, L., Hammarlund, E.U., Bengtson, S., Chaussidon, M., Gauthier-Lafaye, F., Meunier, A., Riboulleau, A., Rollion-Bard, C., Rouxel, O., Asael, D., Pierson-Wickmann, A.-C., El Albani, A., 2013. Oxygen dynamics in the aftermath of the Great Oxidation of Earth's atmosphere. *Proc. Natl. Acad. Sci.* <http://dx.doi.org/10.1073/pnas.1315570110>.

Canfield, D.E., Poulton, S.W., Knoll, A.H., Narbonne, G.M., Ross, G., Goldberg, T., Strauss, H., 2008. Ferruginous conditions dominated later Neoproterozoic deep-water chemistry. *Science* 321, 949–952. <http://dx.doi.org/10.1126/science.1154499>.

Canfield, D.E., Raiswell, R., Westrich, J.T., Reaves, C.M., Berner, R.A., 1986. The use of chromium reduction in the analysis of reduced inorganic sulfur in sediments and shales. *Chem. Geol.* 54, 149–155. [http://dx.doi.org/10.1016/0009-2541\(86\)90078-1](http://dx.doi.org/10.1016/0009-2541(86)90078-1).

Chappaz, A., Lyons, T.W., Gregory, D.D., Reinhard, C.T., Gill, B.C., Li, C., Large, R.R., 2014. Does pyrite act as an important host for molybdenum in modern and ancient euxinic sediments? *Geochim. Cosmochim. Acta* 126, 112–122. <http://dx.doi.org/10.1016/j.gca.2013.10.028>.

Condie, K.C., Des Marais, D.J., Abbott, D., 2001. Precambrian superplumes and supercontinents: a record in black shales, carbon isotopes, and paleoclimates? *Precambrian Res.* 106, 239–260. [http://dx.doi.org/10.1016/S0301-9268\(00\)00097-8](http://dx.doi.org/10.1016/S0301-9268(00)00097-8).

Coplen, T.B., Brand, W.A., Gehre, M., Gröning, M., Meijer, H.A.J., Toman, B., Verkouteren, R.M., 2006. New guidelines for $\delta^{13}C$ measurements. *Anal. Chem.* 78, 2439–2441. <http://dx.doi.org/10.1021/ac052027c>.

Corrigan, D., Pehrsson, S., Wodicka, N., de Kemp, E., 2009. The Palaeoproterozoic Trans-Hudson Orogen: a prototype of modern accretionary processes. *Geol. Soc. Lond. Spec. Publ.* 327, 457–479. <http://dx.doi.org/10.1144/SP327.19>.

Corrigan, D., Scott, D.J., St-Onge, M.R., 2001. Geology of the northern margin of the Trans-Hudson Orogen (Foxe fold belt), central Baffin Island, Nunavut. *Curr. Res. C23*, 1–29.

Craig, J.R., Vokes, F.M., 1993. The metamorphism of pyrite and pyritic ores: an overview. *Mineral. Mag.* 57, 3–18.

Dennen, K.O., Johnson, C.A., Otter, M.L., Silva, S.R., Wandless, G.A., 2006. $\delta^{15}N$ and Non-carbonate $\delta^{13}C$ Values for Two Petroleum Source Rock Reference Materials and a Marine Sediment Reference Material (Open File Report No. 2006-1070). U.S. Geological Survey, Reston, Virginia.

Emerson, S.R., Huested, S.S., 1991. Ocean anoxia and the concentrations of molybdenum and vanadium in seawater. *Mar. Chem.* 34, 177–196. [http://dx.doi.org/10.1016/0304-4203\(91\)90002-E](http://dx.doi.org/10.1016/0304-4203(91)90002-E).

Ferry, J.M., 1981. Petrology of graphitic sulfide-rich schists from South-central Maine; an example of desulfidation during prograde regional metamorphism. *Am. Mineral.* 66, 908–930.

Gagné, S., Jamieson, R.A., MacKay, R., Wodicka, N., Corrigan, D., 2009. Texture, composition, and age variations in monazite from the lower amphibolite to the granulite facies, Longstaff Bluff Formation, Baffin Island, Canada. *Can. Mineral.* 47, 847–869. <http://dx.doi.org/10.3749/canmin.47.4.847>.

German, C.R., Klinkhammer, G.P., Edmond, J.M., Mura, A., Elderfield, H., 1990. Hydrothermal scavenging of rare-earth elements in the ocean. *Nature* 345, 516–518. <http://dx.doi.org/10.1038/345516a0>.

Greber, N.D., Pettke, T., Nägler, T.F., 2014. Magmatic–hydrothermal molybdenum isotope fractionation and its relevance to the igneous crustal signature. *Lithos* 190–191, 104–110. <http://dx.doi.org/10.1016/j.lithos.2013.11.006>.

Guo, Q., Strauss, H., Kaufman, A.J., Schröder, S., Gutzmer, J., Wing, B., Baker, M.A., Bekker, A., Jin, Q., Kim, S.-T., Farquhar, J., 2009. Reconstructing Earth's surface oxidation across the Archean–Proterozoic transition. *Geology* 37, 399–402. <http://dx.doi.org/10.1130/G25423A.1>.

Hanmer, S., Bowring, S., van Breemen, O., Parrish, R., 1992. Great Slave Lake shear zone, NW Canada: mylonitic record of Early Proterozoic continental convergence, collision and indentation. *J. Struct. Geol.* 14, 757–773. [http://dx.doi.org/10.1016/0191-8141\(92\)90039-Y](http://dx.doi.org/10.1016/0191-8141(92)90039-Y).

- Holland, H.D., 1984. *The Chemical Evolution of the Atmosphere and Oceans*. Princeton University Press, Princeton, NJ.
- Holland, H.D., 2003. *The Geologic History of Seawater*. Treatise on Geochemistry. Pergamon, Oxford, pp. 1–46.
- Johns, S.M., Helmstaedt, H.H., Kyser, T.K., 2006. Paleoproterozoic submarine intrabasinal rifting, Baffin Island, Nunavut, Canada: volcanic structure and geochemistry of the Bravo Lake Formation. *Can. J. Earth Sci.* 43, 593–616. <http://dx.doi.org/10.1139/e06-009>.
- Kajiwar, Y., Sasaki, A., Matsubara, O., 1981. Kinetic sulfur isotope effects in the thermal decomposition of pyrite. *Geochem. J.* 15, 193–197. <http://dx.doi.org/10.2343/geochemj.15.193>.
- Karhu, J.A., Holland, H.D., 1996. Carbon isotopes and the rise of atmospheric oxygen. *Geology* 24, 867–870. [http://dx.doi.org/10.1130/0091-7613\(1996\)024<0867:CIATRO>2.3.CO;2](http://dx.doi.org/10.1130/0091-7613(1996)024<0867:CIATRO>2.3.CO;2).
- Kendall, B., Creaser, R.A., Gordon, G.W., Anbar, A.D., 2009. Re–Os and Mo isotope systematics of black shales from the Middle Proterozoic Velkerri and Wollongorang Formations, McArthur Basin, northern Australia. *Geochim. Cosmochim. Acta* 73, 2534–2558. <http://dx.doi.org/10.1016/j.gca.2009.02.013>.
- Kendall, B., Gordon, G.W., Poulton, S.W., Anbar, A.D., 2011. Molybdenum isotope constraints on the extent of late Paleoproterozoic ocean euxinia. *Earth Planet. Sci. Lett.* 307, 450–460. <http://dx.doi.org/10.1016/j.epsl.2011.05.019>.
- Konhauser, K.O., Lalonde, S.V., Planavsky, N.J., Pecoits, E., Lyons, T.W., Mojzsis, S.J., Rouxel, O.J., Barley, M.E., Rosiere, C., Fralick, P.W., Kump, L.R., Bekker, A., 2011. Aerobic bacterial pyrite oxidation and acid rock drainage during the Great Oxidation Event. *Nature* 478, 369–373. <http://dx.doi.org/10.1038/nature10511>.
- Kump, L.R., 2008. The rise of atmospheric oxygen. *Nature* 451, 277–278. <http://dx.doi.org/10.1038/Nature06587>.
- Kump, L.R., Junium, C., Arthur, M.A., Brasier, A., Fallick, A., Melezhik, V., Lepland, A., Črne, A.E., Luo, G., 2011. Isotopic evidence for massive oxidation of organic matter following the Great Oxidation Event. *Science* 334, 1694–1696. <http://dx.doi.org/10.1126/science.1213999>.
- Loukola-Ruskeeniemi, K., 1991. Geochemical evidence for the hydrothermal origin of sulphur, base metals and gold in Proterozoic metamorphosed black shales, Kainuu and Outokumpu areas, Finland. *Miner. Deposita* 26, 152–164. <http://dx.doi.org/10.1007/BF00195262>.
- Luepke, J.J., Lyons, T.W., 2001. Pre-Rodinian (Mesoproterozoic) supercontinental rifting along the western margin of Laurentia: geochemical evidence from the Belt–Purcell Supergroup. *Precambrian Res.* 111, 79–90. [http://dx.doi.org/10.1016/S0301-9268\(01\)00157-7](http://dx.doi.org/10.1016/S0301-9268(01)00157-7).
- Lyons, T.W., Severmann, S., 2006. A critical look at iron paleoredox proxies: new insights from modern euxinic marine basins. *Geochim. Cosmochim. Acta* 70, 5698–5722. <http://dx.doi.org/10.1016/j.gca.2006.08.021>.
- Lyons, T.W., Reinhard, C.T., Planavsky, N.J., 2014. *The rise of oxygen in Earth's early ocean and atmosphere*. *Nature* 506, 307–315.
- Melezhik, V.A., Fallick, A.E., Medvedev, P.V., Makarikhin, V.V., 1999. Extreme ^{13}C carb enrichment in ca. 2.0 Ga magnesite–stromatolite–dolomite–‘red beds’ association in a global context: a case for the world-wide signal enhanced by a local environment. *Earth-Sci. Rev.* 48, 71–120. [http://dx.doi.org/10.1016/S0012-8252\(99\)00044-6](http://dx.doi.org/10.1016/S0012-8252(99)00044-6).
- Neubert, N., Nägler, T.F., Böttcher, M.E., 2008. Sulfidity controls molybdenum isotope fractionation into euxinic sediments: evidence from the modern Black Sea. *Geology* 36, 775–778. <http://dx.doi.org/10.1130/G24959A.1>.
- Noordmann, J., Weyer, S., Montoya-Pino, C., Dellwig, O., Neubert, N., Eckert, S., Paetzel, M., Böttcher, M.E., 2015. Uranium and molybdenum isotope systematics in modern euxinic basins: case studies from the central Baltic Sea and the Kyllaren fjord (Norway). *Chem. Geol.* 396, 182–195. <http://dx.doi.org/10.1016/j.chemgeo.2014.12.012>.
- Oliver, N.H.S., Hoering, T.C., Johnson, T.W., Rumble III, D., Shanks III, W.C., 1992. Sulfur isotopic disequilibrium and fluid–rock interaction during metamorphism of sulfidic black shales from the Waterville–Augusta area, Maine, USA. *Geochim. Cosmochim. Acta* 56, 4257–4265. [http://dx.doi.org/10.1016/0016-7037\(92\)90266-L](http://dx.doi.org/10.1016/0016-7037(92)90266-L).
- Partin, C.A., Bekker, A., Corrigan, D., Modeland, S., Francis, D., Davis, D.W., 2014. Sedimentological and geochemical basin analysis of the Paleoproterozoic Penrhyn and Piling groups of Arctic Canada. *Precambrian Res.* 251, 80–101. <http://dx.doi.org/10.1016/j.precambres.2014.06.010>.
- Partin, C.A., Bekker, A., Planavsky, N.J., Scott, C.T., Gill, B.C., Li, C., Podkovyrov, V., Maslov, A., Konhauser, K.O., Lalonde, S.V., Love, G.D., Poulton, S.W., Lyons, T.W., 2013. Large-scale fluctuations in Precambrian atmospheric and oceanic oxygen levels from the record of U in shales. *Earth Planet. Sci. Lett.* 369–370, 284–293. <http://dx.doi.org/10.1016/j.epsl.2013.03.031>.
- Pearce, C.R., Cohen, A.S., Coe, A.L., Burton, K.W., 2008. Molybdenum isotope evidence for global ocean anoxia coupled with perturbations to the carbon cycle during the Early Jurassic. *Geology* 36, 231–234. <http://dx.doi.org/10.1130/G24446A.1>.
- Planavsky, N.J., Reinhard, C.T., 2014. *Deep Ocean Oxygenation (Presented at the Goldschmidt, Sacramento)*. p. 1965.
- Planavsky, N.J., Bekker, A., Hofmann, A., Owens, J.D., Lyons, T.W., 2012. Sulfur record of rising and falling marine oxygen and sulfate levels during the Lomagundi event. *Proc. Natl. Acad. Sci.* 209, 18300–18305. <http://dx.doi.org/10.1073/pnas.1120387109>.
- Planavsky, N.J., McGoldrick, P., Scott, C.T., Li, C., Reinhard, C.T., Kelly, A.E., Chu, X., Bekker, A., Love, G.D., Lyons, T.W., 2011. Widespread iron-rich conditions in the mid-Proterozoic ocean. *Nature* 477, 448–451. <http://dx.doi.org/10.1038/nature10327>.
- Planavsky, N.J., Reinhard, C.T., Wang, X., Thomson, D., McGoldrick, P., Rainbird, R.H., Johnson, T., Fischer, W.W., Lyons, T.W., 2014. Low Mid-Proterozoic atmospheric oxygen levels and the delayed rise of animals. *Science* 346, 635–638. <http://dx.doi.org/10.1126/science.1258410>.
- Pope, M.C., Grotzinger, J.P., 2003. Paleoproterozoic Stark Formation, Athapuscow Basin, Northwest Canada: record of cratonic-scale salinity crisis. *J. Sediment. Res.* 73, 280–295. <http://dx.doi.org/10.1306/091302730280>.
- Poulton, R.L., Siebert, C., McManus, J., Berelson, W.M., 2006. Authigenic molybdenum isotope signatures in marine sediments. *Geology* 34, 617–620. <http://dx.doi.org/10.1130/G22485.1>.
- Poulton, S.W., Canfield, D.E., 2005. Development of a sequential extraction procedure for iron: implications for iron partitioning in continentally derived particulates. *Chem. Geol.* 214, 209–221. <http://dx.doi.org/10.1016/j.chemgeo.2004.09.003>.
- Poulton, S.W., Canfield, D.E., 2011. Ferruginous conditions: a dominant feature of the ocean through Earth's history. *Elements* 7, 107–112. <http://dx.doi.org/10.2113/gselements.7.2.107>.
- Poulton, S.W., Fralick, P.W., Canfield, D.E., 2004. The transition to a sulphidic ocean 1.84 billion years ago. *Nature* 431, 173–177. <http://dx.doi.org/10.1038/nature02912>.
- Poulton, S.W., Fralick, P.W., Canfield, D.E., 2010. Spatial variability in oceanic redox structure 1.8 billion years ago. *Nat. Geosci.* 3, 486–490. <http://dx.doi.org/10.1038/Ngeo889>.
- Rainbird, R.H., Davis, W.J., Pehrsson, S.J., Wodicka, N., Rayner, N., Skulski, T., 2010. Early Paleoproterozoic supracrustal assemblages of the Rae domain, Nunavut, Canada: intracratonic basin development during supercontinent break-up and assembly. *Precambrian Res.* 181, 167–186. <http://dx.doi.org/10.1016/j.precambres.2010.06.005>.
- Raiswell, R., 1982. Pyrite texture, isotopic composition and the availability of iron. *Am. J. Sci.* 282, 1244–1263. <http://dx.doi.org/10.2475/ajs.282.8.1244>.
- Raiswell, R., Berner, R.A., 1986. Pyrite and organic matter in Phanerozoic normal marine shales. *Geochim. Cosmochim. Acta* 50, 1967–1976. [http://dx.doi.org/10.1016/0016-7037\(86\)90252-8](http://dx.doi.org/10.1016/0016-7037(86)90252-8).
- Rasmussen, B., Fletcher, I.R., Bekker, A., Muhling, J.R., Gregory, C.J., Thorne, A.M., 2012. Deposition of 1.88-billion-year-old iron formations as a consequence of rapid crustal growth. *Nature* 484, 498–501. <http://dx.doi.org/10.1038/nature11021>.
- Reinhard, C.T., Lyons, T.W., Rouxel, O., Asael, D., Dauphas, N., Kump, L., 2013a. *Iron Speciation and Isotope Perspectives on Paleoproterozoic Water Column Chemistry*. In: Melezhik, V.A., Kump, L.R., Fallick, A.E., Strauss, H., Hanski, E.J., Prave, A.R., Lepland, A. (Eds.), *Reading the Archive of Earth's Oxygenation*. Springer, pp. 1483–1492.
- Reinhard, C.T., Planavsky, N.J., Robbins, L.J., Partin, C.A., Gill, B.C., Lalonde, S.V., Bekker, A., Konhauser, K.O., Lyons, T.W., 2013b. Proterozoic ocean redox and biogeochemical stasis. *Proc. Natl. Acad. Sci.* 110, 5357–5362. <http://dx.doi.org/10.1073/pnas.1208622110>.
- Reuschel, M., Melezhik, V.A., Strauss, H., 2012a. Sulfur isotopic trends and iron speciation from the c. 2.0 Ga Pilgūjärvi Sedimentary Formation, NW Russia. *Precambrian Res.* 196–197, 193–203. <http://dx.doi.org/10.1016/j.precambres.2011.12.009>.
- Reuschel, M., Melezhik, V.A., Whitehouse, M.J., Lepland, A., Fallick, A.E., Strauss, H., 2012b. Isotopic evidence for a sizeable seawater sulfate reservoir at 2.1 Ga. *Precambrian Res.* 192–195, 78–88. <http://dx.doi.org/10.1016/j.precambres.2011.10.013>.
- Ripley, E.M., Snyder, K., 2000. Experimental sulfur isotope studies of the pyrite to pyrrhotite conversion in a hydrogen atmosphere. *Econ. Geol.* 95, 1551–1554. <http://dx.doi.org/10.2113/gsecongeo.95.7.1551>.
- Sahoo, S.K., Planavsky, N.J., Kendall, B., Wang, X., Shi, X., Scott, C., Anbar, A.D., Lyons, T.W., Jiang, G., 2012. Ocean oxygenation in the wake of the Marinoan glaciation. *Nature* 489, 546–549. <http://dx.doi.org/10.1038/nature11445>.
- Schidlowski, M., 2001. Carbon isotopes as biogeochemical recorders of life over 3.8 Ga of Earth history: evolution of a concept. *Precambrian Res.* 106, 117–134. [http://dx.doi.org/10.1016/S0301-9268\(00\)00128-5](http://dx.doi.org/10.1016/S0301-9268(00)00128-5).
- Schröder, S., Bekker, A., Beukes, N.J., Strauss, H., Van Niekerk, H.S., 2008. Rise in seawater sulphate concentration associated with the Paleoproterozoic positive carbon isotope excursion: evidence from sulphate evaporites in the ~2.2–2.1 Gyr shallow-marine Lucknow Formation, South Africa. *Terra Nova* 20, 108–117. <http://dx.doi.org/10.1111/j.1365-3121.2008.00795.x>.
- Scott, C., Lyons, T.W., Bekker, A., Shen, Y., Poulton, S.W., Chu, X., Anbar, A.D., 2008. Tracing the stepwise oxygenation of the Proterozoic ocean. *Nature* 452, 456–459. <http://dx.doi.org/10.1038/nature06811>.
- Scott, D.J., St-Onge, M.R., Corrigan, D., 2002. *Geology of the Paleoproterozoic Piling Group and underlying Archean gneiss, central Baffin Island, Nunavut*. *Curr. Res.* C17, 1–10.
- Scott, C., Wing, B.A., Bekker, A., Planavsky, N.J., Medvedev, P., Bates, S.M., Yun, M., Lyons, T.W., 2014. Pyrite multiple-sulfur isotope evidence for rapid expansion and contraction of the early Paleoproterozoic seawater sulfate reservoir. *Earth Planet. Sci. Lett.* 389, 95–104. <http://dx.doi.org/10.1016/j.epsl.2013.12.010>.
- Shen, Y., Knoll, A.H., Walter, M.R., 2003. Evidence for low sulphate and anoxia in a mid-Proterozoic marine basin. *Nature* 423, 632–635.
- Siebert, C., Nägler, T.F., Kramers, J.D., 2001. Determination of molybdenum isotope fractionation by double-spike multicollector inductively coupled plasma mass spectrometry. *Geochim. Geophys. Geosyst.* 2, 1032. <http://dx.doi.org/10.1029/2000GC000124>.
- Siebert, C., Nägler, T.F., von Blanckenburg, F., Kramers, J.D., 2003. Molybdenum isotope records as a potential new proxy for paleoceanography. *Earth Planet. Sci. Lett.* 211, 159–171. [http://dx.doi.org/10.1016/S0012-821X\(03\)00189-4](http://dx.doi.org/10.1016/S0012-821X(03)00189-4).
- Slack, J.F., Grenne, T., Bekker, A., Rouxel, O.J., Lindberg, P.A., 2007. Suboxic deep seawater in the late Paleoproterozoic: evidence from hematitic chert and iron formation related to seafloor–hydrothermal sulfide deposits, central Arizona, USA. *Earth Planet. Sci. Lett.* 255, 243–256. <http://dx.doi.org/10.1016/j.epsl.2006.12.018>.
- Sun, S., McDonough, W.F., 1989. Chemical and isotopic systematics of oceanic basalts: implications for mantle composition and processes. *Geol. Soc. Lond. Spec. Publ.* 42, 313–345. <http://dx.doi.org/10.1144/GSL.SP.1989.042.01.19>.
- Taylor, S.R., McLennan, S.M., 1985. *The Continental Crust: Its Composition and Evolution*. Blackwell Scientific Pub., Oxford.
- Tippett, C.R., 1978. A detailed cross-section through the southern margin of the Foxe Fold Belt in the vicinity of Dewar Lakes, Baffin Island, District of Franklin. *Curr. Res. Pap.* 78-1A, 169–173.
- Tribouillard, N., Algeo, T.J., Lyons, T., Riboulleau, A., 2006. Trace metals as paleoredox and paleoproductivity proxies: an update. *Chem. Geol.* 232, 12–32. <http://dx.doi.org/10.1016/j.chemgeo.2006.02.012>.
- Valley, J.W., 1986. *Stable isotope geochemistry of metamorphic rocks*. *Rev. Mineral. Geochem.* 16, 445–489.

- Voegelin, A.R., Pettke, T., Greber, N.D., von Niederhäusern, B., Nägler, T.F., 2014. Magma differentiation fractionates Mo isotope ratios: evidence from the Kos Plateau Tuff (Aegean Arc). *Lithos* 190–191, 440–448. <http://dx.doi.org/10.1016/j.lithos.2013.12.016>.
- Wodicka, N., St-Onge, M.R., Corrigan, D., Scott, D.J., Whalen, J.B., 2014. Did a proto-ocean basin form along the southeastern Rae cratonic margin? Evidence from U–Pb geochronology, geochemistry (Sm–Nd and whole-rock), and stratigraphy of the Paleoproterozoic Piling Group, northern Canada. *Geol. Soc. Am. Bull.* <http://dx.doi.org/10.1130/B31028.1>.
- Wodicka, N., St-Onge, M.R., Scott, D.J., Corrigan, D., 2002. Preliminary Report on the U–Pb Geochronology of the Northern Margin of the Trans-Hudson Orogen, Central Baffin Island (Current Research No. 2002-F7). Radiogenic age and isotopic studies: report 15. Geological Survey of Canada.
- Yamamoto, M., 1984. Sulfur isotope effects in the thermal breakdown of pyrite. *Earth Planet. Sci. Lett.* 69, 335–340. [http://dx.doi.org/10.1016/0012-821X\(84\)90192-4](http://dx.doi.org/10.1016/0012-821X(84)90192-4).